Master's Thesis

Overcoming parasitic reactions occurring in carbonaceous Seawater Battery cathodes and their mechanisms

Wonsuk Lee

School of Energy and Chemical Engineering

(Battery Science and Technology)

Ulsan National Institute of Science and Technology

2021

Overcoming parasitic reactions occurring in carbonaceous Seawater Battery cathodes and their mechanisms

Wonsuk Lee

School of Energy and Chemical Engineering

(Battery Science and Technology)

Ulsan National Institute of Science and Technology

Overcoming parasitic reactions occurring in carbonaceous Seawater Battery cathodes and their mechanisms

A thesis/dissertation submitted to
Ulsan National Institute of Science and Technology
in partial fulfillment of the
requirements for the degree of
Master of Science

Wonsuk Lee

12/08/2020

Approved by

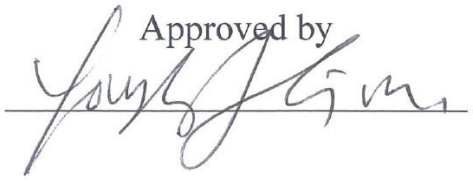

Advisor
Youngsik Kim

Overcoming parasitic reactions occurring in carbonaceous Seawater Battery cathodes and their mechanisms

Wonsuk Lee

This certifies that the thesis/dissertation of Wonsuk Lee is approved.

12/08/2020

Signature

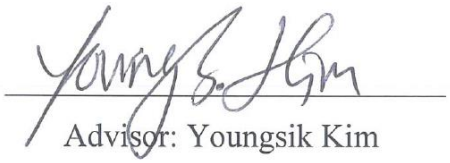

Advisor: Youngsik Kim

Signature

Seok Ju Kang

Signature

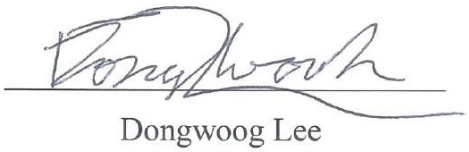

Dongwoog Lee

Abstract

Rechargeable seawater batteries (SWBs) have recently been investigated as a potential candidate for future energy storage systems, owing to their cost-effectiveness and environmentally friendly properties derived from the use of naturally abundant seawater as a catholyte. However, the fundamental understanding of the cathode reactions in SWBs is not yet fully elucidated; hence, an investigation of their mechanisms is imperative for future development. Herein, parasitic cathode reactions other than the previously identified oxygen evolution/reduction reactions (OERs/ORRs) are identified for the first time using activated carbon cloth (ACC) as the cathode current collector. In this study, carbon fibers of the current collector were observed to undergo cathode side-reactions such as fiber-fracturing carbon corrosion during charging and surface-insulating $CaCO_3$ precipitation via carbon dioxide capture during discharging, both resulting in cathode performance failure. Moreover, carbon corrosion was determined to be the dominant factor behind performance degradation under normal charge–discharge cycling conditions in comparison to $CaCO_3$ precipitation, which was found to be a reversible phenomenon during the operation of the SWB. These results provide insight for future work into enhancing the longevity of SWBs by identifying carbon corrosion as the main cathode performance degradation mechanism. Owing to these findings, an alternative cathode which exceeds the performance and cycle stability of the previously investigated ACC was found. An activated carbon fiber (ACF) cathode with a larger degree of graphitization than the ACC was found to resist carbon corrosion. Characterization and comparison of the level of carbon disorder in the ACC and ACF was done, elucidating the origin of the difference in carbon corrosion resistance.

Contents

List of Figures

List of Tables

I. Introduction

1.1 Energy Storage Systems

With the ever-increasing demand for energy consumption, environmental concerns such as global warming and pollution due to fossil fuels are becoming a constant issue, making the exploitation of renewable energy sources such as wind and solar energy generation a necessity. In this regard, energy storage systems (ESSs) are of immense interest as a means to provide constant energy storage and supply owing to their compatibility with renewable energy, with various utility-scale functions such as peak shaving and frequency regulation.[1-4] As a result, the rapid expansion of the ESS market can be currently observed as a global trend with an annual market size increase expectancy from $59 billion (164 GWh) in 2019 to $546 billion (3046 GWh) in 2035.[5]

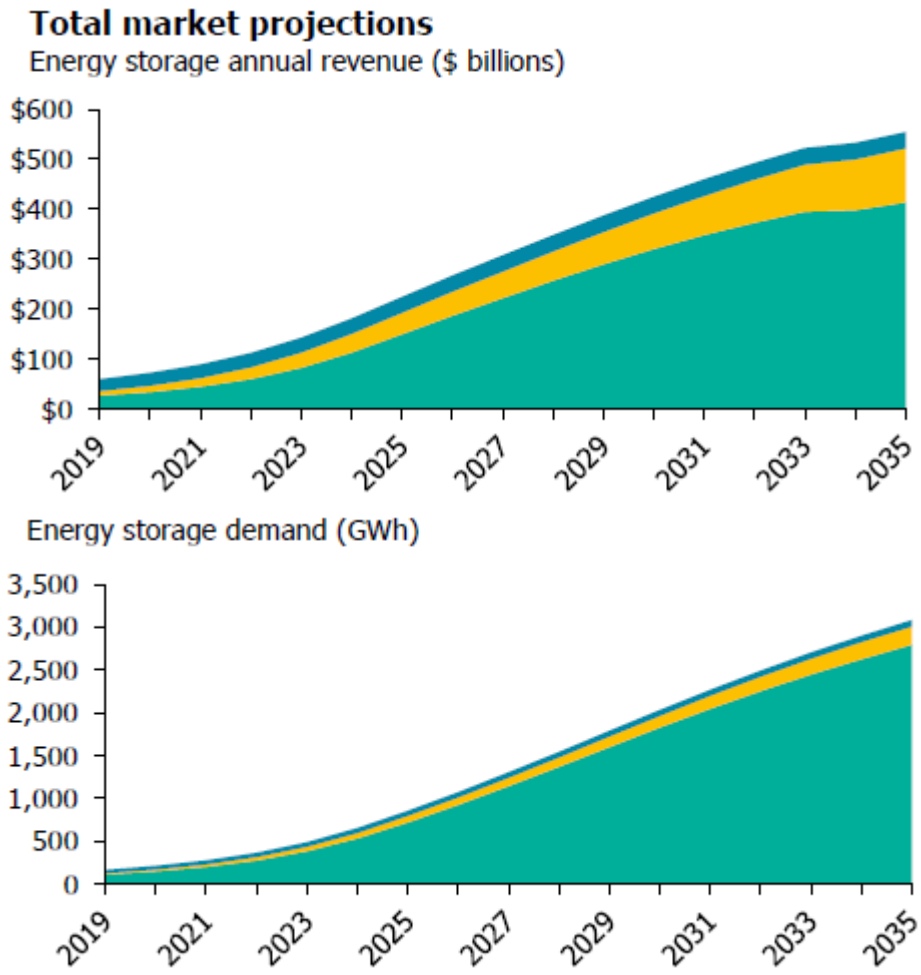

Figure 1 Global energy storage revenue and demand forecast

Traditionally, mechanical/kinetic ESS technologies such as Pumped Hydro Storage (PHS), Compressed Air Energy Storage (CAES), Flywheel Energy Storage (FES) has been used as a method for storing energy charged from baseload generating power plants. These technologies provided the bulk storage for industrial purposes, with PHS constituting as the largest baseload capacity.

PHS technology is a method for storing and supplying electricity at high peak demands via moving bulk water between two interconnected reservoirs with different heights.[6] Energy production in PHS relies on water flowing through a turbine at the final outlet, and typically provides power in the megawatt range capacity. The economic life span of the PHS ranges from 50 to 100 years and has an advantage in terms of relatively low additional expenses in comparison with battery based ESS (BESS) with enormous maintenance costs. However, disadvantages such as the long construction period, high initial investment cost, environmental destruction risks, limited construction areas due to geographical constraints, disconnection of the ecosystem, and the high power loss due to the long supply distance from the power plant to the consumer has to be taken into account.

CAES is a method of compressing and storing air, and then rotating a turbine with compressed air to generate power.[7] In general, large-scale compressed air energy storage technology produces compressed air during low power demand, stores it in an underground cave, etc., and pulls it up at a time when power is needed to generate power by rotating a turbine. In the process of compressing air using a compressor, a lot of heat is generated, and the temperature decreases during the expansion process of generating power using a turbine. To prevent moisture in the air from freezing and affecting the turbine or other parts, air is heated before it is supplied to the turbine.

The FES is a device that rotates a motor using excess power, storing the inertial energy of the attached rotating body at this time, and converting it back to electric energy during necessary periods.[8] The advantage of this system is that it has excellent energy storage efficiency in comparison to existing mechanical and chemical energy storage devices, can charge and discharge instantaneously, has a semi-permanent lifespan, and is eco-friendly without waste materials that is hazardous to the environment. As such, traditional technologies such as PHS, CAES, and FES are suitable for large-scale MW/GW level energy storage but are limited by the geographical environment of the installation site.

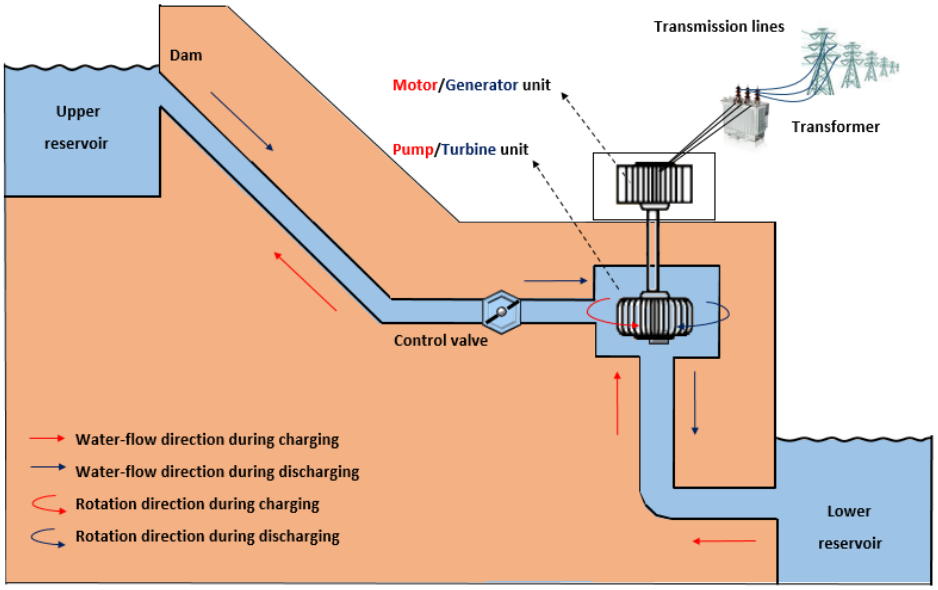

Figure 2 Schematic of a Pumped Hydro Storage (PHS) energy storage system

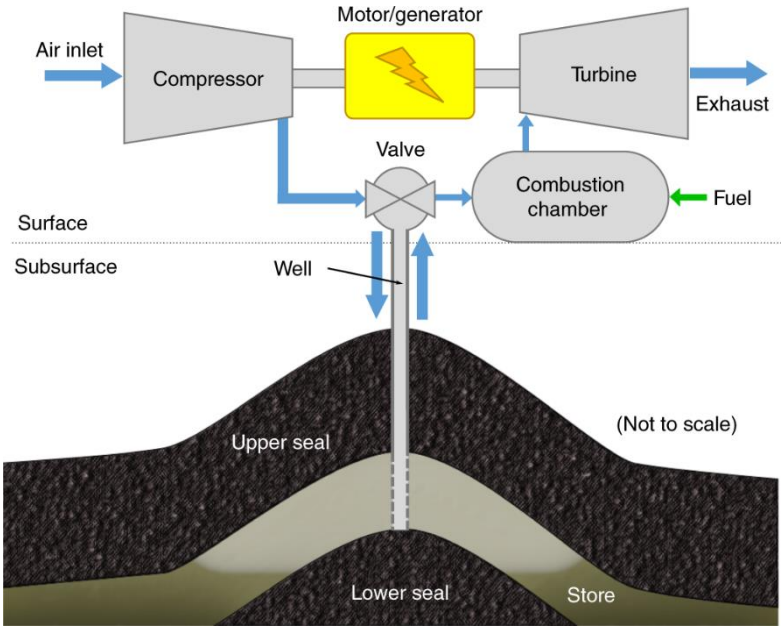

Figure 3 Schematic of a Compressed Air Energy Storage (CAES) system

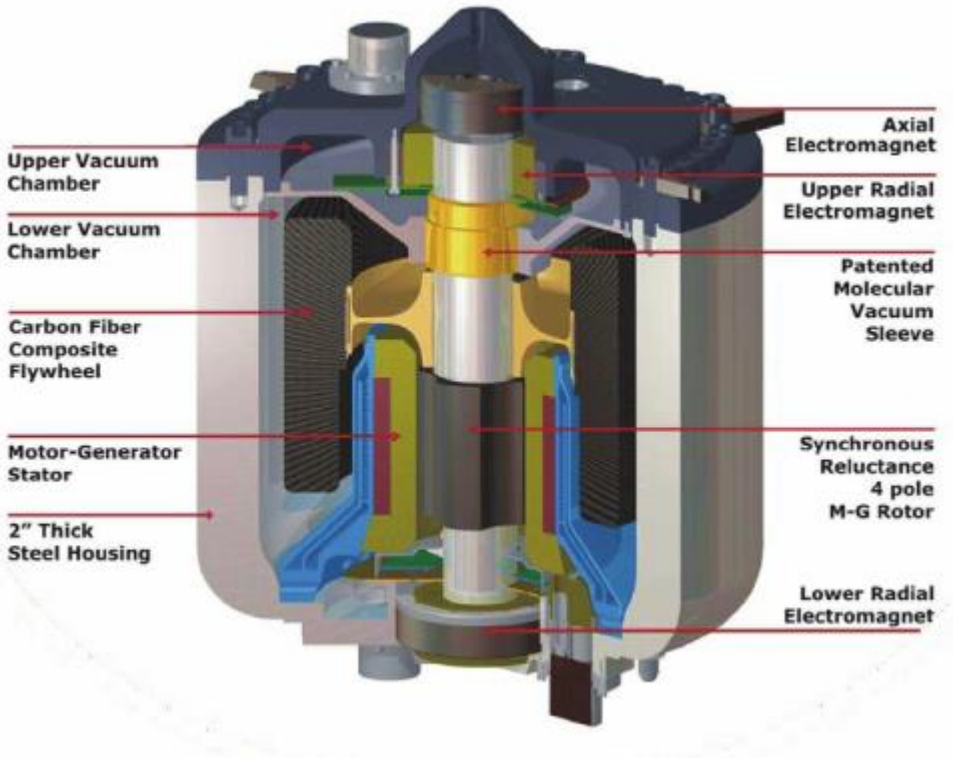

Figure 4 Schematic of a Flywheel Energy Storage (CAES) system

Other battery based ESS technologies (BESS) also exist due to their compatibility with the grid in terms of frequency regulation, owing to their ability to provide small-scale power quickly in sudden change scenarios. BESS are operated based on electrochemical principles to store energy, and numerous types of technologies exist such as the Lead-Acid battery (LAB), Sodium-Sulfur (NaS), Redox Flow Batteries (RFB), and lithium ion batteries (LIB).[9] Lead-acid batteries are inexpensive and have the advantage of being strong against overcharging, but their disadvantages include short lifespan characteristics, low energy density, and generation of hazardous substances. Lead-acid batteries have the longest history in terms of actual usage, but their usage is currently decreasing due to the disadvantages listed above. NaS batteries are suitable for large-scale power storage systems due to their large capacity and have high-efficiency charging/discharging characteristics, but they must maintain high temperatures for charging/discharging, resulting in an inherent risk of explosion. Unlike conventional secondary batteries, redox flow batteries are charged/discharged by the oxidation/reduction of the active material in the electrolyte. It has the advantage of having a long life, large-capacity usage, and few restrictions on the installation location, but its low efficiency due to a low energy density is a disadvantage.[10] Lithium secondary batteries are the most excellent batteries among secondary batteries that are currently commercially available and are mainly used in portable products such as smart phones, notebook computers, and various household devices such as power tools due to their high energy density. Moreover, with the expansion of the new and renewable energy industry and the expansion of the electric vehicle market, interest in enhancing the capacity of lithium secondary batteries with excellent performance is increasing, and research is being actively conducted accordingly.[11]

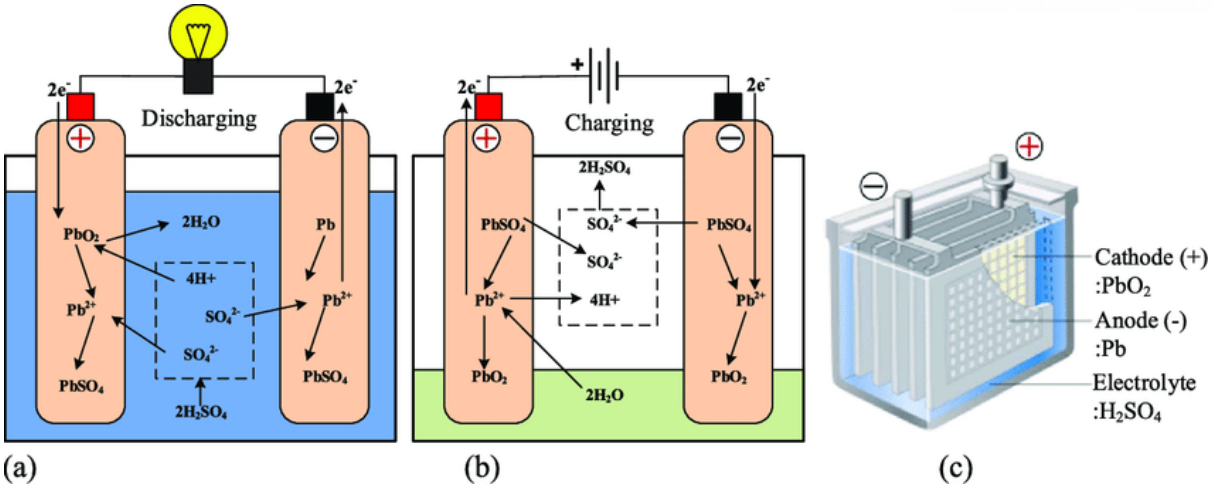

Figure 5 Schematic of a Lead-Acid Battery system

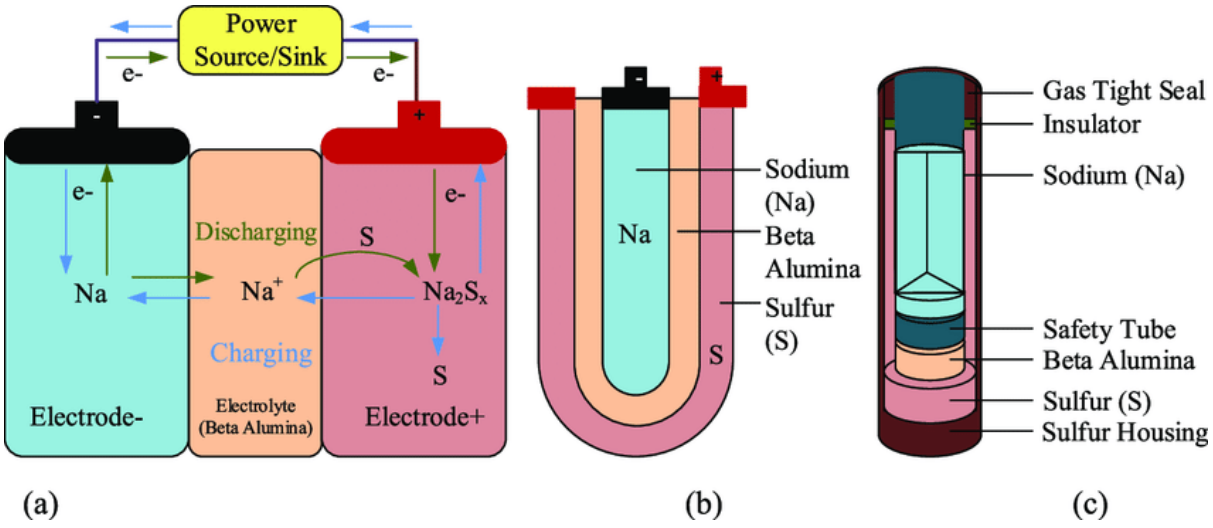

Figure 6 Schematic of a Sodium-Sulfur Battery system

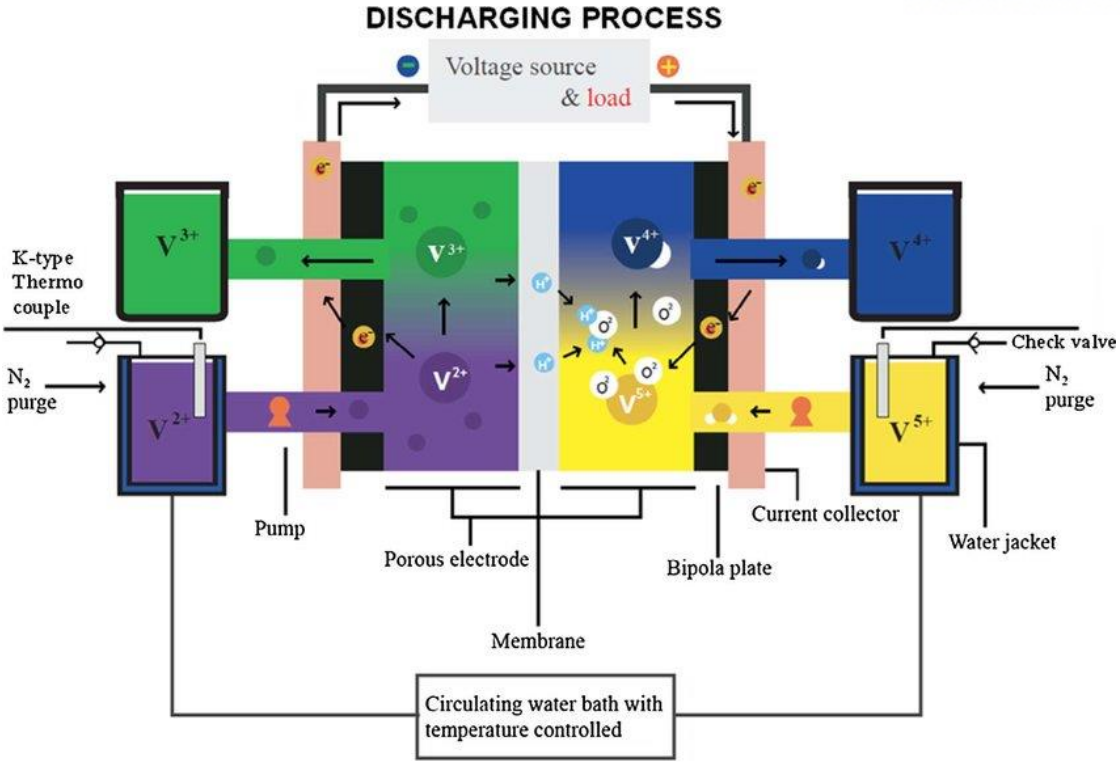

Figure 7 Schematic of a Vanadium Redox Flow Battery (VRFB) system

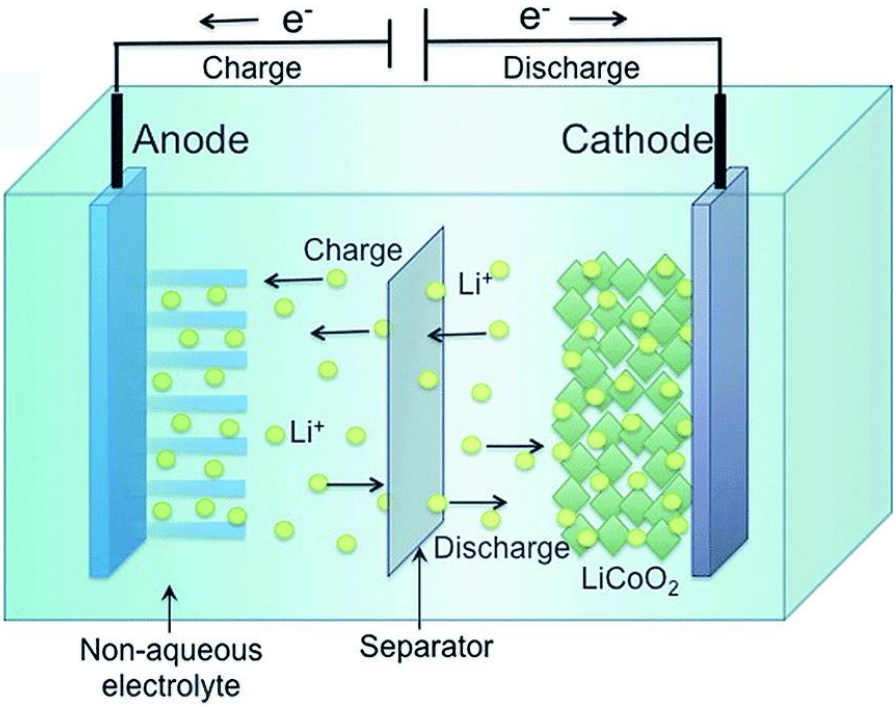

Figure 8 Schematic of a Lithium-ion Battery (LIB) system

Among the numerous different types of BESS technologies, rechargeable Li-ion batteries (LIBs) are the most widely used in various application fields owing to their long cycle lifetime, high energy, and power density.[12-16] However, there are limitations to using the reserves of lithium and cobalt in terms of sustainability, due to their low abundance in the earth's crust, necessitating alternative rechargeable battery systems.[17-19] In this regard, a novel electrochemical storage system that utilizes naturally abundant seawater as the catholyte and sodium source, termed the "seawater battery" (SWB), is recently being recognized as a promising alternative.[20-23]

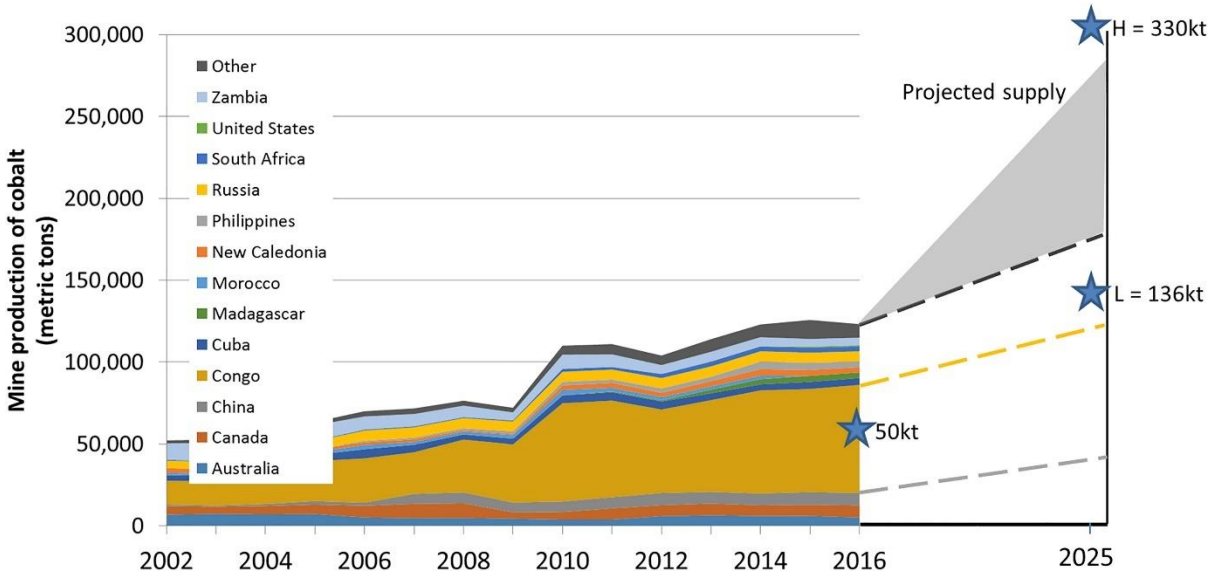

Figure 9 Estimated projection in the increase for cobalt production

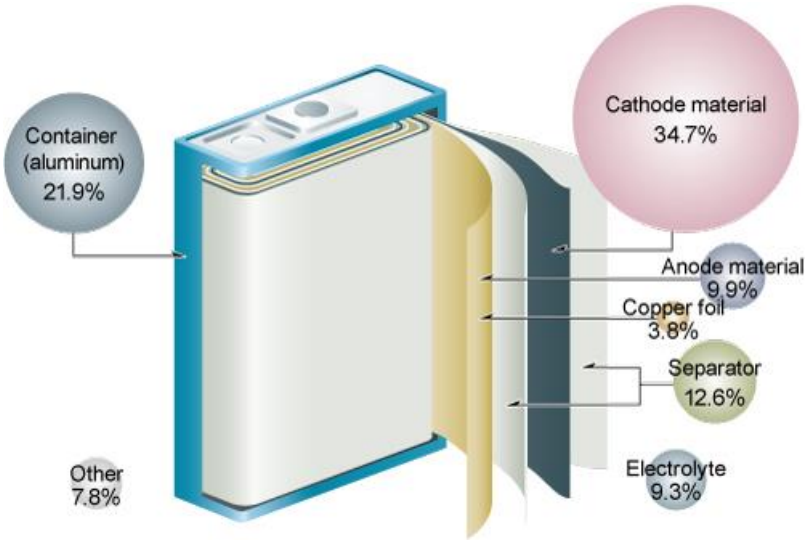

Figure 11 LIB component cost comparison

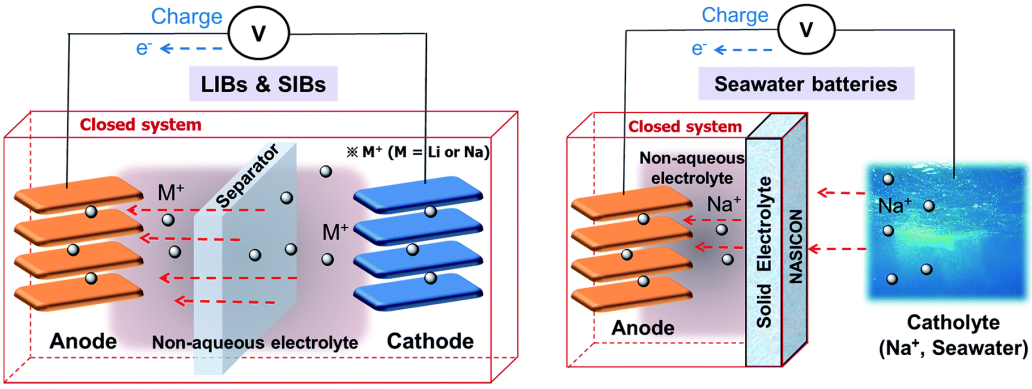

Figure 10 Comparison between Seawater Batteries and Lithium Ion Batteries

1.2 Seawater Batteries

SWBs have potential to be used as a method for energy storage especially in marine applications, due to their intrinsic ability to use sodium ions in natural seawater as a cathode active material source. As marine environmental regulations such as greenhouse has regulations set by the International Maritime Organization (IMO) are strengthened, the demand for eco-friendly energy technology is required, and it is necessary to present and foster long-term development paradigm shifts towards reducing fossil fuels and greenhouse gas emissions. In this aspect, SWBs uses its positive electrode as natural seawater, reducing the cost by more than 1/3 compared to lithium ion batteries, and by more than 16% in the case of omitting the electrode manufacturing process. Moreover, SWBs have advantages in terms of safety due to the use of natural seawater as a cooling agent, and the use of solid electrolyte which enhances the safety of the SWB, minimizing the need for additional facilities for heat management. It also does not contain chemicals such as F, S, and N, which are harmful to the environment in case of fire or cell decomposition, so it is less flammable, harmful, and reactive compared to other batteries, making it environmental and user-friendly. Due to the listed advantages above, the SWB is promising in terms of its usage for marine applications such as smart ICT buoy systems, sonar buoys, marine navigation beacons, and auxiliary power sources for ships.

In terms of working principles, SWBs are composed of a Na metal anode within a non-aqueous anolyte and a cathode current collector within the open structured seawater catholyte, both of which are physically separated by a Na-ion conducting $Na_3Zr_2Si_2PO_{12}$ (NASICON) ceramic membrane. Fig. 12 shows a schematic of the seawater battery and Fig. 15 shows the digital photographs for the actual experimental setup. As shown in the illustration, Na^+ ions existing in seawater are transported through the NASICON membrane to the anode side during charging, while oxygen evolution reactions (OER) takes place at the cathode. Conversely, the Na^+ ions are transported back to the cathode during discharging while oxygen reduction reactions (ORR) occur at the cathode. Following each of the half-cell reactions at the anode (eqn (1)) and the cathode (eqn (2)), the net theoretical potential of the seawater battery can be given as E°~3.48V vs Na/Na^+ (eqn (3)) at pH = 8. Here, the OER and ORR occurring at the cathode current collector are key electrochemical processes that determine the overall cell performance, indicating the importance of the search for suitable cathode materials.

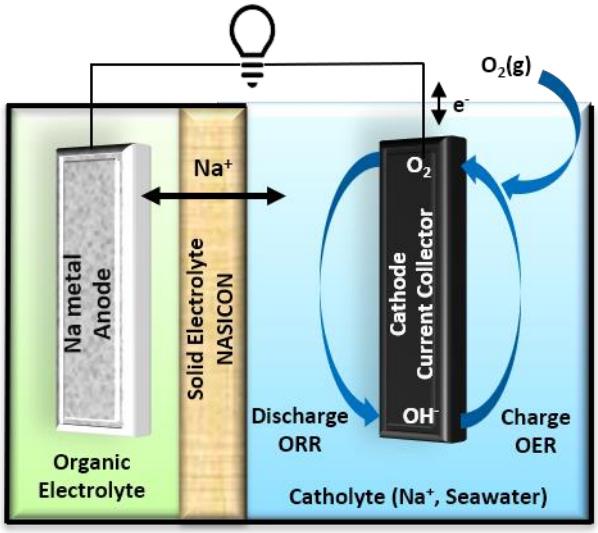

Figure 12 Schematic illustration showing cell components and electrochemical charge discharge mechanism of seawater batteries

$Na^+ + e^- \leftrightarrow Na$; E° = -2.73V vs NHE (1)

$O_2 + 2H_2O + 4e^- \leftrightarrow 4OH^-$; E° = 0.75V vs NHE (pH = 8) (2)

$4Na(s) + 2H_2O + O_2(aq) \leftrightarrow 4NaOH(aq)$; E ° = 3.48V vs Na/Na^+ (pH = 8) (3)

1.3 Research Proposal

Accordingly, carbonaceous materials have previously been investigated as a candidate for cathode current collectors in SWBs due to their stability in seawater, high electrical conductivity, good electrochemical stability, large surface area, and cost-effectiveness.[24, 25] However, SWBs exhibit an increased voltage gap (0.6V to 1.42V) and a decreased energy efficiency (83% to 64%) when using an activated carbon cloth (ACC) as the cathode current collector, after 80 cycles at a current of 0.25mA (0.13mA cm^{-2}) for 5h at each step, as shown in Fig. 13. Moreover, the gradual increase of overpotential even in early cycles and the voltage efficiency restoration after the replacement of the cathode in Fig. 14 implies that the cathode is the main site for cell performance degradation and may have different degradation processes: (1) Surface carbon oxidation resulting in gradual impedance build-up and (2) structural damage after a critical operation time.

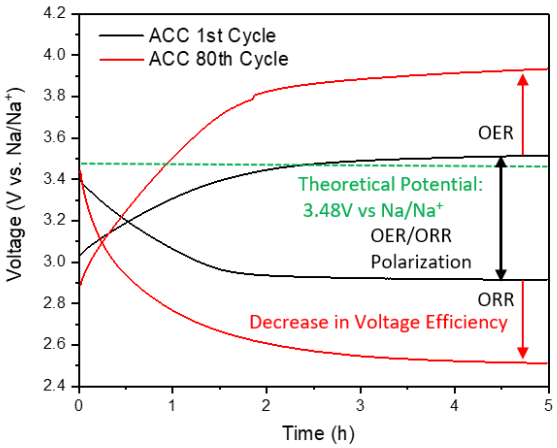

Figure 13 Galvanostatic charge-discharge voltage profile comparison at 1st and 80th cycle with ACC current collector showing increased polarization after repeated cycling

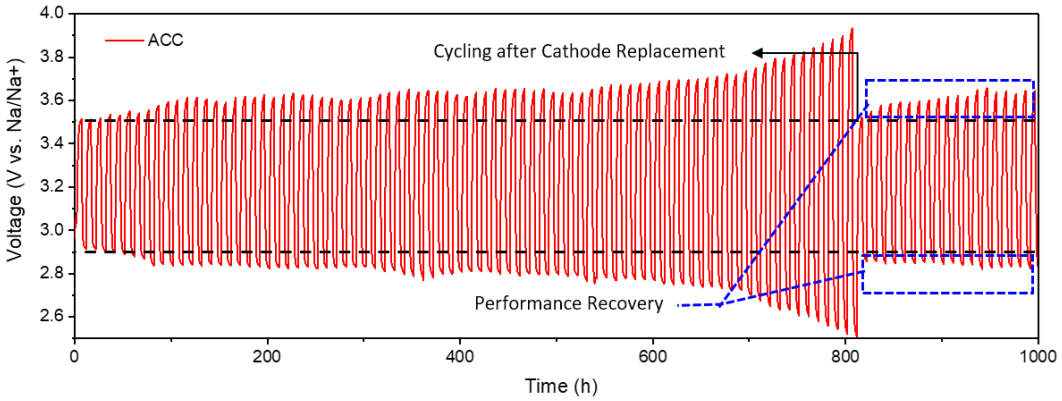

Figure 14 Cycle performance at 0.25mA (0.13mA cm^{-2}) for 5h at each step showing performance recovery after cathode replacement.

Despite these results and previous studies in related fields identifying undesired side-reactions accompanying the desired OER/ORR at the carbon cathode as the cause for performance failure, a lack of understanding still exists regarding the cathode performance degradation in SWBs. In more detail, carbon corrosion was found to occur as a side-reaction in fuel cells[26-33] during start-up/shut-down conditions and vanadium redox flow batteries[34-38] during charging conditions, both due to their usage of carbonaceous electrodes in oxidizing situations. Additionally, $CaCO_3$ precipitation on the electrode surface was found to occur as a side-reaction in primary magnesium-based SWBs due to the occurrence of the ORR in a seawater environment at discharging conditions.[39, 40]

These systems are akin to the rechargeable SWB system in terms of their identical choice of carbonaceous electrode material or ORR cathode reaction in seawater environments, marking carbon corrosion and $CaCO_3$ precipitation as a highly probable cause for performance degradation in SWBs. Hence, the ascertainment of these assumed cathode side-reactions and their impact in SWB systems is a vital for future considerations on cycle stability issues.

In this study, we have investigated the failure mechanisms of an ACC cathode current collector in SWB systems, which were found to be due to the cathode side-reactions occurring during the charge and discharge procedures instead of the desired target reactions, the OER and ORR. Carbon corrosion was identified to occur as a side-reaction during charging through *in-situ* chronopotentiometry with differential electrochemical mass spectroscopy (DEMS), scanning electron microscopy (SEM), X-ray photoelectron spectroscopy (XPS) and N_2 adsorption-desorption isotherms. Similarly, $CaCO_3$ precipitation during discharge was observed through X-ray powder diffraction (XRD), SEM, XPS, and N_2 adsorption-desorption isotherms. The impact of both side-reactions on the cell performance was observed through electrochemical tests. An additional experiment utilizing a three-electrode configuration with two cathodes and an anode was conducted to mimic actual cycle conditions. Each cathode was physically decoupled so that each was involved separately in charge and discharge, enabling the identification of the individual side-reaction.

Our results indicate that carbon corrosion is the dominant reason for performance failure in actual operating conditions, whereas $CaCO_3$ precipitation is a reversible process and the precipitate can be dissolved away to not significantly affect cell performance.

II. Experimental

2.1 Cell assembly

The cathode current collector for this study was fabricated by simply cutting the Activated Carbon Cloth (ACC; ACC-5092-20, Kynol) into a round disk with a diameter of 16mm for all experiments, with no further treatments due to its intrinsic hydrophilic property. Vacuum filtrated natural seawater from Ilsan beach, Ulsan, Republic of Korea was used as the catholyte for this work. The coin-cell type anode part was assembled in a glove box under an Ar atmosphere with the following procedures. First, the solid electrolyte (NASICON, $Na_3Zr_2Si_2PO_{12}$), which was prepared by our previously reported method, was cut into a diameter of 16mm and attached to a polypropylene cap. Na metal (99.9%, Sigma Aldrich) was then attached to a stainless steel spacer as the anode, which was placed on top of the NASICON with a polyethylene separator (Celgard) positioned in between to prevent direct contact. Finally, an organic electrolyte of 1M $NaCF_3SO_3$ in tetraethylene glycol dimethyl ether (TEGDME) solvent was injected before sealing the coin cell. A flow-cell tester (4TOONE Energy Co., Ltd) filled with 200mL of vacuum filtrated natural seawater was used to integrate the fabricated anode coin-cell and the cathode for all experiments.

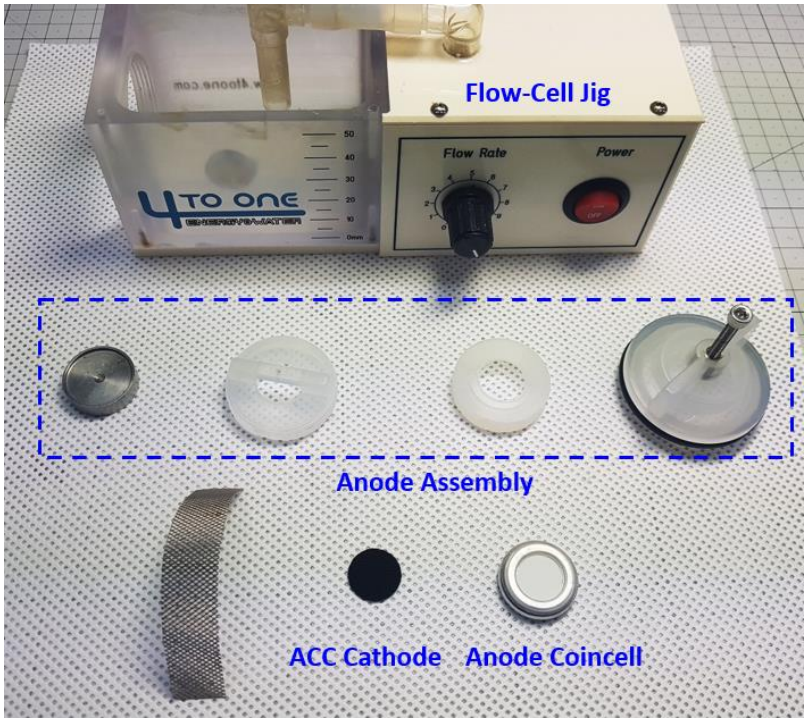

Figure 15 Photographs of components of the experimental setup for seawater battery cell performance evaluation

2.2 Material Characterization

Scanning electron microscopy (SEM) images and energy-dispersive X-ray spectroscopy (EDS) mapping were carried out on an S-4800 electron microscope (Hitachi High-Technologies, 10kV, 7uA) to observe the impact of side-reactions on the surface of the ACC cathode. X-ray photoelectron spectroscopy (XPS) analysis of the ACC cathode was conducted by the ESCLAB 250XI (Thermo Fisher Scientific) spectrometer with monochromatic Al Kα X-ray sources (1486.7 eV). X-ray diffraction (XRD) patterns of the formed precipitates on the ACC surface after discharge were characterized by using the D8 Advance (Bruker AXS) diffractometer using Cu Kα radiation (40mA, 40kV) at interval steps of 0.02 ranging from 10° to 80°. Specific surface area and pore size distribution of the ACC were determined through N_2 adsorption-desorption isotherms at 77K by the BELSORP-Max physisorption analyzer (BEL Japan) using the Brunauer–Emmett–Teller (BET) and Barrett-Joyner-Halenda (BJH) method. Raman spectroscopy was used to compare the degree of graphitization in the ACC and ACF cathode by calculating the I_d/I_g ratio by the Alpha300S AFM-Raman analyzer (WITec).

2.3 Electrochemical Characterization

The charge-discharge performance for SWBs using ACC as the cathode was tested using the WonATech battery testing system (WBCS 3000) with a current of 0.25mA (0.13mA cm^{-2}) for varying periods. The Biologic electrochemical workstation (VSP-300) was used to conduct cyclic voltammetry (CV) and polarization curves through a three-electrode configuration with Ag/AgCl as the reference electrode, platinum coil as a counter electrode, ACC as the working electrode and seawater as the electrolyte. A modified three-electrode setup composed of two cathodes and one anode was additionally used to identify individual side-reactions at normal cycling conditions. A differential electrochemical mass spectrometer (DEMS) was used to identify CO_2 evolution during the charging process, and its detailed setups are described elsewhere and is shown in Figure 16.[41, 42] An ORION Star A216 pH meter (Thermo Fisher Scientific) was in-situ used to track the pH change during the charging process.

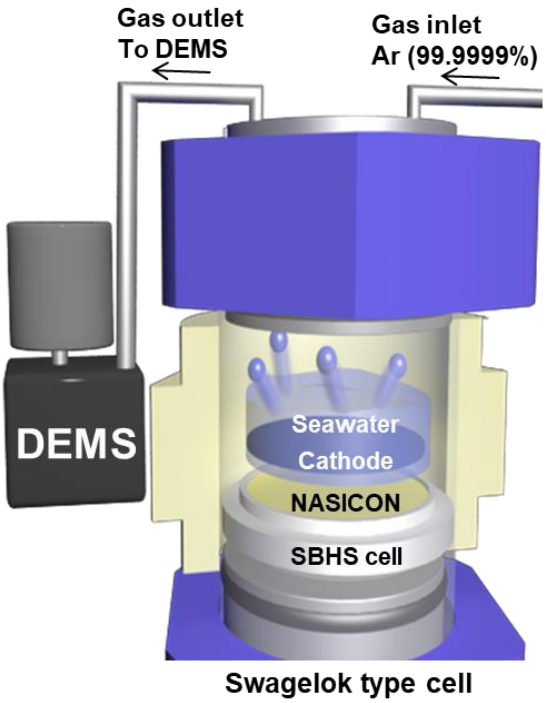

Figure 16 Schematic of a DEMS setup for SWBs

III. Results and discussion

3.1 Cathode side-reactions during charging

Carbon corrosion was first confirmed to have occurred as a side-reaction by monitoring the gas evolution with DEMS during the galvanostatic charging of the SWB cell at a current of 0.25mA (0.13mA cm^{-2}), as shown in Fig. 17. The resulting CO_2 gas evolution corresponds to the final product of the carbon corrosion reaction (eqn (4)-(6)), where the surface carbon of the ACC cathode is oxidized owing to the thermodynamic instability of carbon under the aqueous seawater environment at high electrochemical potentials.

$$C + H_2O \rightarrow CO_2 + 4H^+ + 4e^- \; ; \; E^\circ = 0.207V \text{ vs NHE} \quad (4)$$

$$C + H_2O \rightarrow CO + 2H^+ + 2e^- \; ; \; E^\circ = 0.518V \text{ vs NHE} \quad (5)$$

$$CO + H_2O \rightarrow CO_2 + 2H^+ + 2e^- \; ; \; E^\circ = -0.103V \text{ vs NHE} \quad (6)$$

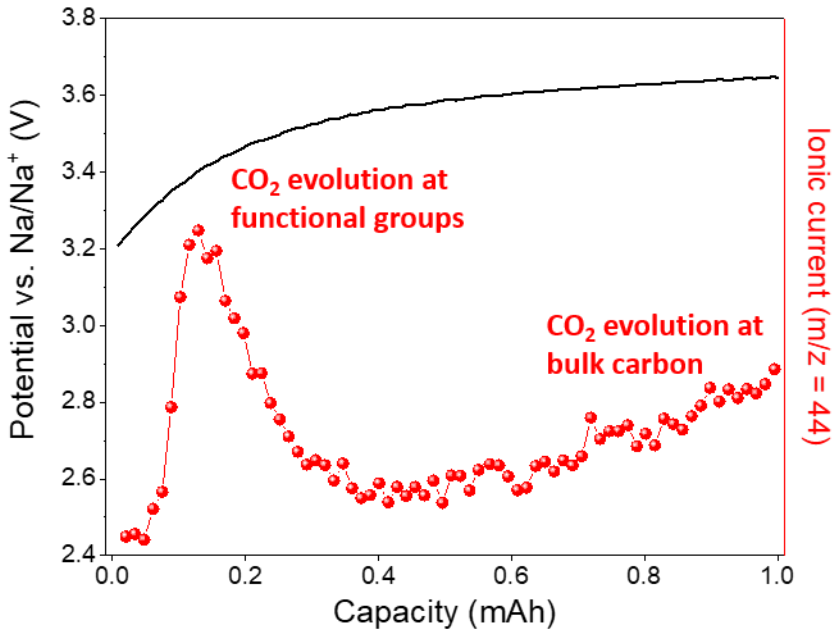

Figure 17 CO_2 evolution detection by differential electrochemical mass spectroscopy (DEMS) during galvanostatic charging of the ACC current collector at 0.25mA (0.13mA cm^{-2})

Carbon fibers exposed to a higher positive potential than the standard potential undergo surface oxidation starting from the edges and corners of its basal planes, which are more susceptible to electrochemical corrosion; further, the oxygenated surface carbon species are decomposed to CO_2 while acting as intermediates for the corrosion mechanism.[43, 44] Overall, the rate of carbon corrosion is determined both from the morphology and surface functional groups of the ACC cathode. Hence, the appearance of an initial peak of CO_2 evolution from Fig. 17 at around 0.1mAh of charging corresponds to the rapid decomposition of the more-susceptible edge sites and functional groups, followed by a continual increase of gas evolution due to corrosion at the bulk carbon.

To investigate the physical effects of carbon corrosion on the cathode structure, the morphology and microstructure change of the ACC cathode fibers were observed through SEM images. Although no visible difference due to carbon corrosion can be seen from the digital photographs in Fig. 18, the magnified SEM images clearly shows the effects of carbon corrosion on the ACC cathode. The ACC cathode itself is composed of bundles of uniformly oriented microsized carbon fibers with numerous nanosized pores on its surface. Fig. 19 shows low- and high-magnification SEM images of the ACC cathode after being pre-charged for 20mAh. In comparison to the original pristine fibers from the inset, the corroded fibers show overall alteration and erosion of its structure. Portions of the surface can be seen being peeling off from the fiber, and reduced connectivity *via* fracturing effects on its main body can also be observed. These structural changes by carbon corrosion can be expected to induce negative impacts on cell performance, such as a decrease in the specific surface area *via* peeling and loss of electrical conductivity *via* fracturing. Fig. 20 also features an EDS mapping image of a charged ACC, showing that the atomic composition is based solely on C and O after carbon corrosion, indicating no external solid species from seawater have attached to the surface of the ACC in any form whatsoever.

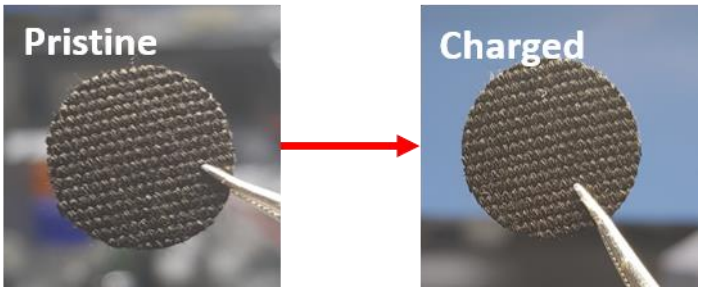

Figure 18 Digital photographs of ACC before and after charging

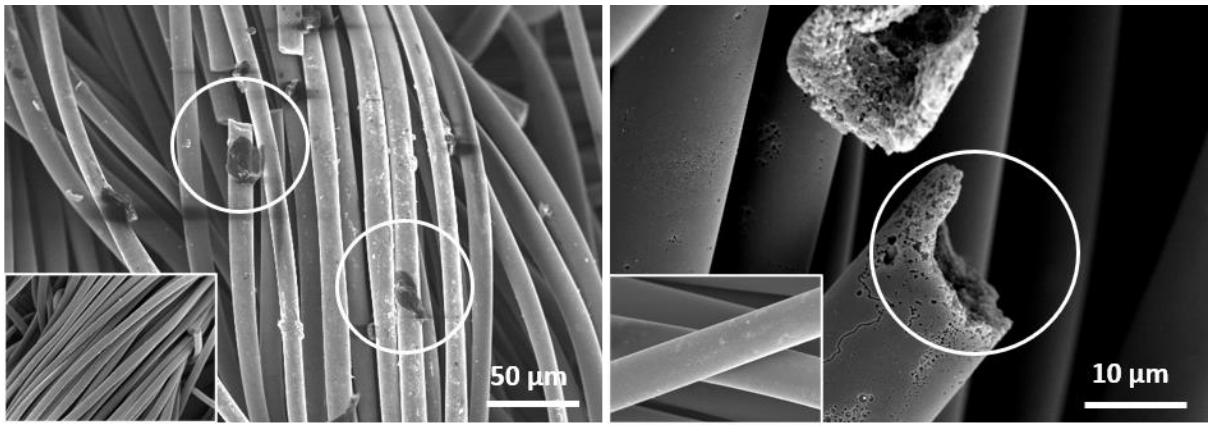

Figure 19 SEM images of 20mAh pre-charged ACC showing surface peeling and fiber fracture with inset images of pristine ACC of the same resolution.

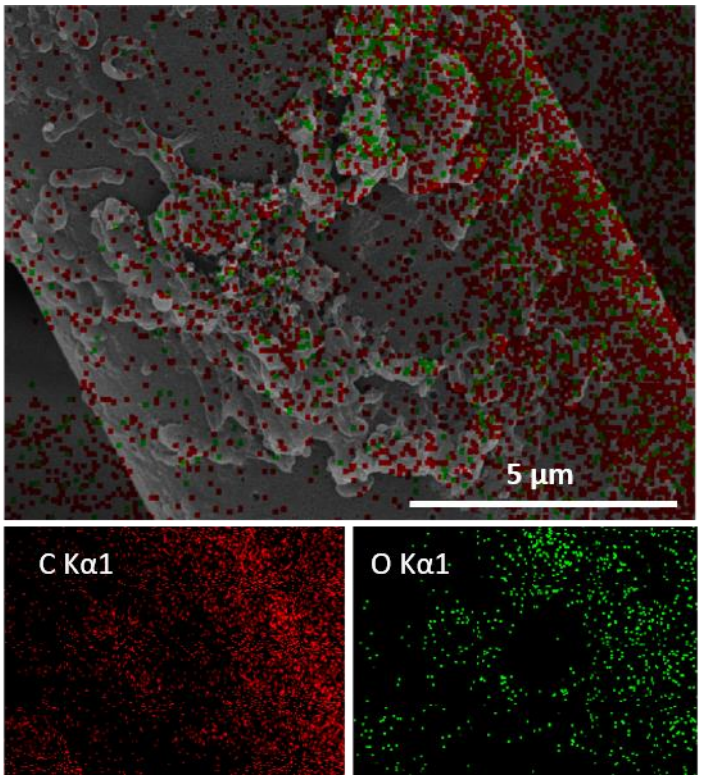

Figure 20 EDS mapping images of charged ACC showing fiber peeling along with oxygen species on their surface

Nitrogen adsorption/desorption isotherms of the pristine and pre-charged ACC samples are shown in Fig. 21 to further elucidate the effect of carbon corrosion on the BET specific surface area and pore size distribution. The ACC cathode was pre-charged 20mAh in advance in an SWB cell to artificially aggravate the carbon corrosion reaction, to compare its characteristics with a pristine ACC sample. A typical Type I isotherm indicating a microporous structure can be observed for both cases, corresponding to the SEM image in the inset showing the porous surface of the pristine ACC.[45] As a result, the ACC can be seen to possess a very high specific surface area of 2078m2g-1 and a mean pore diameter of 1.72nm, indicating that it is a very suitable cathode due to its relatively abundant surface reaction sites. Comparing the isotherms of the pristine and pre-charged ACC, however, it can be seen that the adsorbed volume is greatly reduced after the charging process, indicating that carbon corrosion has decreased its specific surface area to 1286m2g-1 and its mean pore diameter to 1.66nm. This reduction of the surface area likely implies that carbon corrosion as a side-reaction during charging will undermine its capability as an SWB cathode, consequently deteriorating the cell performance.

Table 1 Numerical values of the specific surface area, total pore volume, mean pore diameter of the ACC before and after charging via BET

BET method	Pristine ACC	Charged ACC
Specific surface area ($m^2\ g^{-1}$)	2038	1286
Total pore volume ($cm^3\ g^{-1}$)	0.89	0.53
Mean pore diameter (nm)	1.76	1.66

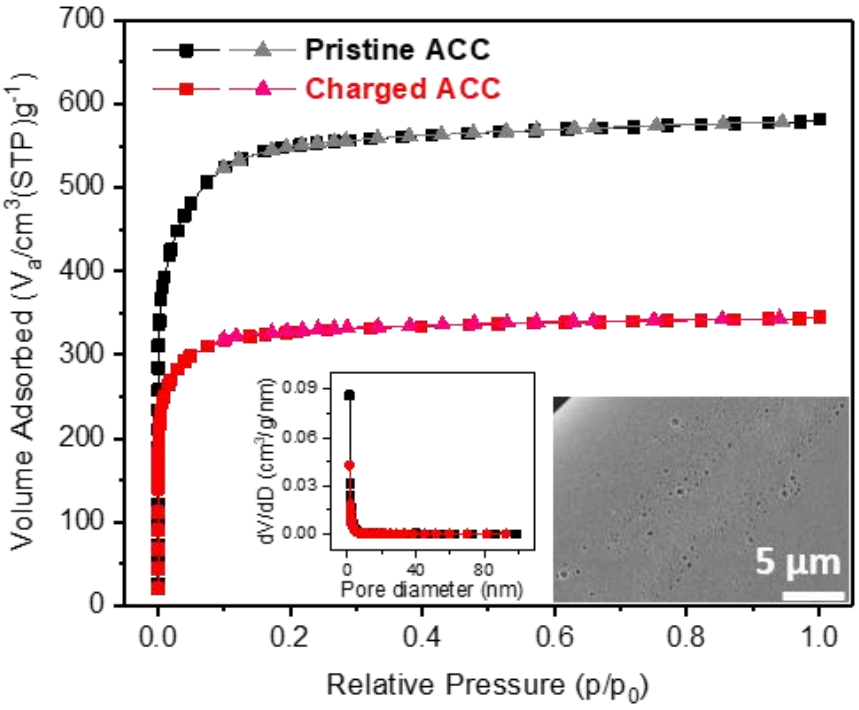

Figure 21 Comparison between pristine and 20mAh charged ACC by N_2 adsorption-desorption isotherms, pore size distribution and SEM image showing the porous surface of pristine ACC (inset).

XPS surface analysis technique was also carried out to analyze the change in the surface functional groups on the surface of the ACC cathode when it undergoes carbon corrosion. The survey spectra of the ACC cathodes before and after charging for 20mAh are shown for comparison in Fig. 22, where the C1s and O1s peaks are predominant. Other minor peaks including S2p, N1s, Na1s, and Mg1s appearing after charging of the ACC are expected to be attributed from the naturally existing ions in residual seawater. An evident increase in the O1s peak and decrease in the C1s peak can be seen from the spectra after charging, indicating the increase of surface oxygen species content on the ACC surface after electrochemical oxidation. This degree of oxygenation can be determined from the O/C atomic ratio of the XPS peaks, which can be used to give quantitative insight into the extent of carbon corrosion. The resulting increase of the O/C atomic ratio from 4.7% (C1s 95.48%, O1s 4.52%) to 40.3% (C1s 64.47%, O1s 25.98%) after charging indicates nearly a tenfold increase in the surface oxygen content *via* carbon corrosion. From the XPS analysis, this increase in the surface oxygen content after charging can be verified to correspond with the oxidizing behavior of carbon corrosion occurring as a side reaction.

Table 2 Numerical values of the carbon, oxygen content of the ACC before and after charging via XPS

Atomic %	Pristine ACC	Charged ACC
C1s	95.48	64.47
O1s	4.52	25.98

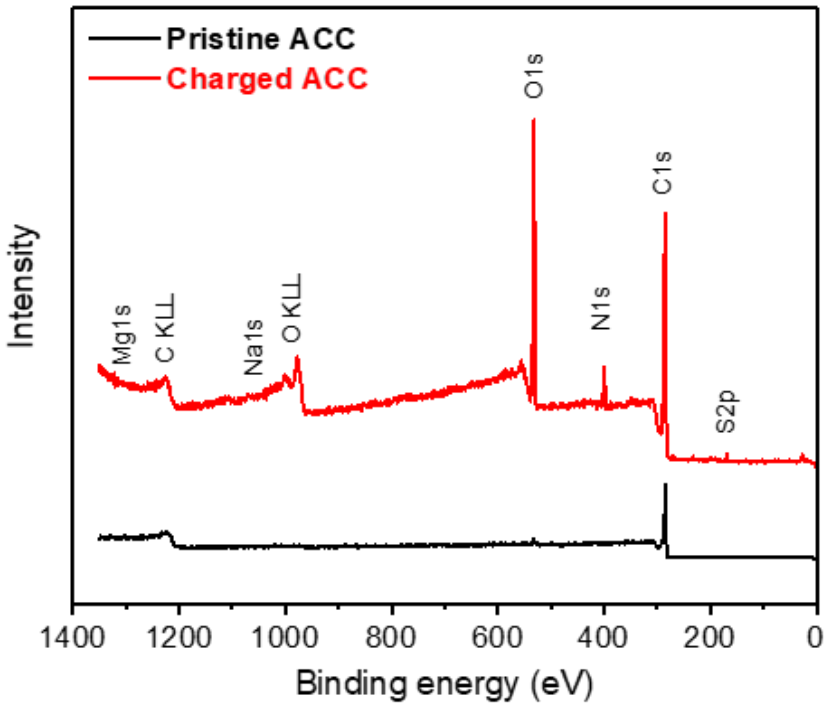

Figure 22 XPS spectra comparison showing increased oxygen species after charging.

The electrochemical performances of the ACC cathode before and after pre-charging were compared by assembling SWB cells for galvanostatic charge tests. The charge tests were conducted by applying a current of 0.25mA(0.13mAcm^{-2}) for 5h and their voltage profiles are shown in Fig. 23. In comparison to a pristine ACC cathode, the 20mAh pre-charged ACC cathode exhibited an increased voltage plateau, from 3.51V to 3.66V from the charge profile, indicating that the degree of polarization was increased after being pre-charged in advance. CV of the ACC cathodes before and after pre-charging was conducted in a range from -0.5V to 1.0V (vs Ag/AgCl) at a scan rate of 0.2mVs^{-1} to examine the effect of carbon corrosion on its electrochemically active surface area (ECSA) *via* the three-electrode method. As shown in Fig. 24, the pristine cathode initially shows a clear capacitive behavior with the formation of an electrical double layer (EDL) region as identified in previous works due to its large surface area. In contrast, the loss of ECSA and EDL after pre-charging is evident in comparison to the pristine cathode, as the current area between the cathodic and anodic curve is drastically decreased. The current density at the apex of the CV curve, as seen, also decreased from an initial 0.89 mAcm^{-2} to 0.11 mAcm^{-2} in the case of OER and increased from an initial -0.72 mAcm^{-2} to -0.14 mAcm^{-2} in ORR, indicating the reduction in electrochemical activity. This decrease in surface area and electrochemical activity occurs due to the unwanted carbon corrosion reaction occurring as a side-reaction during the charging of the SWB. In detail, the conversion of solid carbon to CO_2 gas *via* the carbon corrosion reaction has been previously identified in this paper to induce carbon fiber fracturing and specific surface area reduction, corresponding to the CV results. These results indicate that carbon corrosion led to the performance deterioration of the ACC cathode.

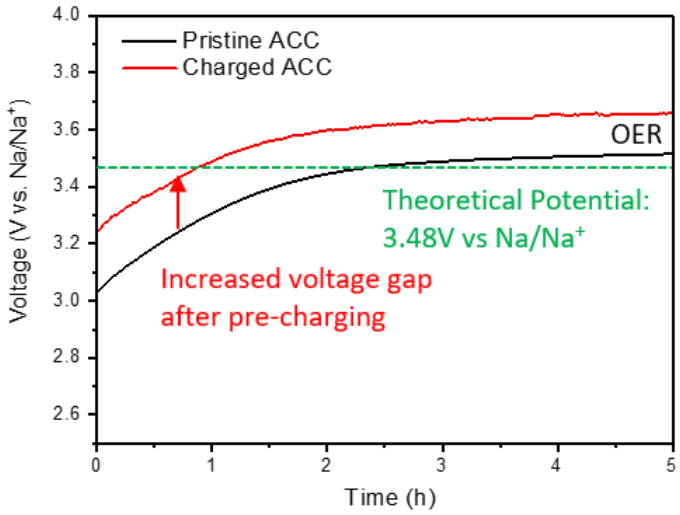

Figure 23 Galvanostatic charge voltage profile comparison at 0.25mA (0.13mA cm^{-2}) for 5h

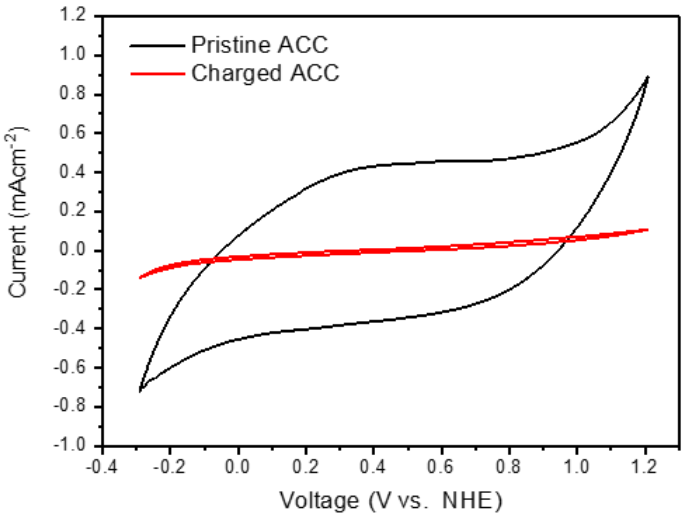

Figure 24 Cyclic voltammograms at a scan rate of 0.2mVs^{-1}

3.2 Cathode side-reactions during discharging

Identification of $CaCO_3$ precipitation as a side-reaction during the discharge of the SWB cell was conducted via XRD analysis. Fig. 25 shows a digital photograph of the ACC sample, captured to identify the precipitates formed on the surface after discharging for 20mAh. The XRD peaks obtained from the precipitates on the discharged ACC cathode surface are shown in Fig 4a and are in good agreement with the aragonite phase of calcium carbonate, in reference to the diffraction pattern (ICDD card 00-041-1475) fitted from High-Score Plus. The formation of aragonite-phase $CaCO_3$ precipitates can be explained from the series of processes described in (eqn (7)-(9)) and Fig. 27, and occurs due to a combination of carbon dioxide circulation in seawater and the ORR, which captures the dissolved carbon dioxide at the cathode during discharge. In more detail, the hydroxide ions created as a product of discharge from (eqn (2)) increase the pH of seawater in the vicinity of the ACC cathode, shifting the carbonic acid equilibria of Fig. 28 from bicarbonate to carbonate ions. The formed carbonate ions, in turn, combine with the naturally existing cations in seawater to form a variety of carbonate solids as in Table 1, predominantly resulting in calcium carbonate due to its lowest solubility and standard Gibbs free energy of formation.[46-48]

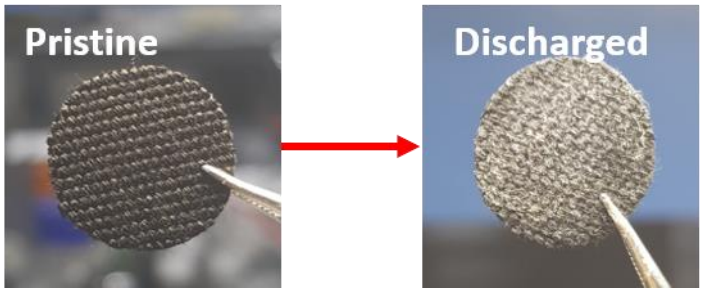

Figure 25 Digital photographs of ACC before and after charging

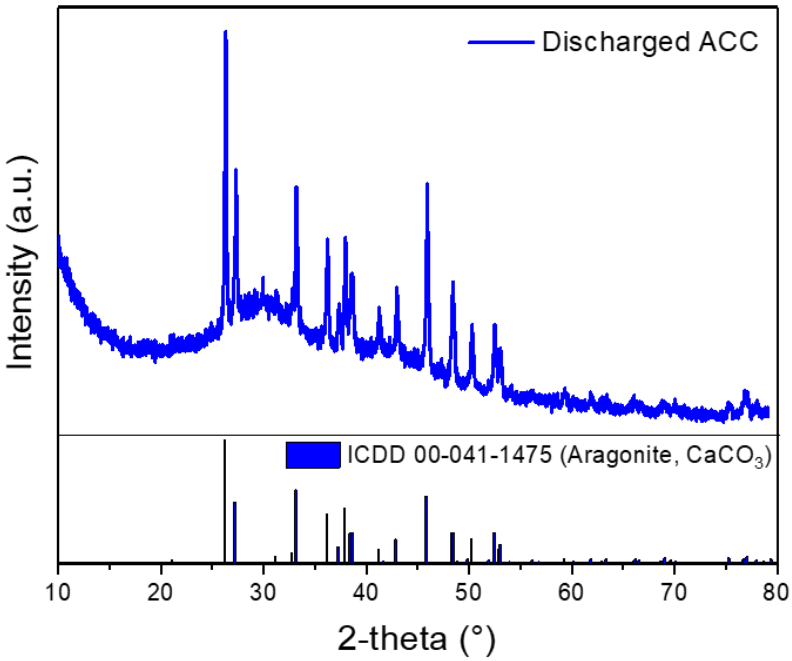

Figure 26 XRD pattern analysis of the formed precipitates on the surface of discharged ACC, with the bottom panel showing the reference diffraction pattern of $CaCO_3$ (Aragonite phase)

$$CO_2 + H_2O \leftrightarrow H_2CO_3 \leftrightarrow H^+ + HCO_3^- \quad (7)$$

$$HCO_3^- + OH^- \rightarrow CO_3^{2-} + H_2O \quad (8)$$

$$Ca^{2+} + CO_3^{2-} \rightarrow CaCO_3\,(s) \quad (9)$$

Table 3 Concentration of cations dominantly existing in seawater and their solubility at carbonate solid phases.

Cations in seawater	Na	Mg	K	Ca
ppm	11 000	1300	500	400
Carbonate solid	Na_2CO_3	$MgCO_3$	K_2CO_3	$CaCO_3$ (aragonite)
Standard Gibbs free energy of formation	−1047.6 kJ mol^{-1}	−1012.1 kJ mol^{-1}	−1064.4 kJ mol^{-1}	−1127.8 kJ mol^{-1}
Solubility at room temperature	307 g L^{-1}	0.106 g L^{-1}	1110 g L^{-1}	0.006 g L^{-1}

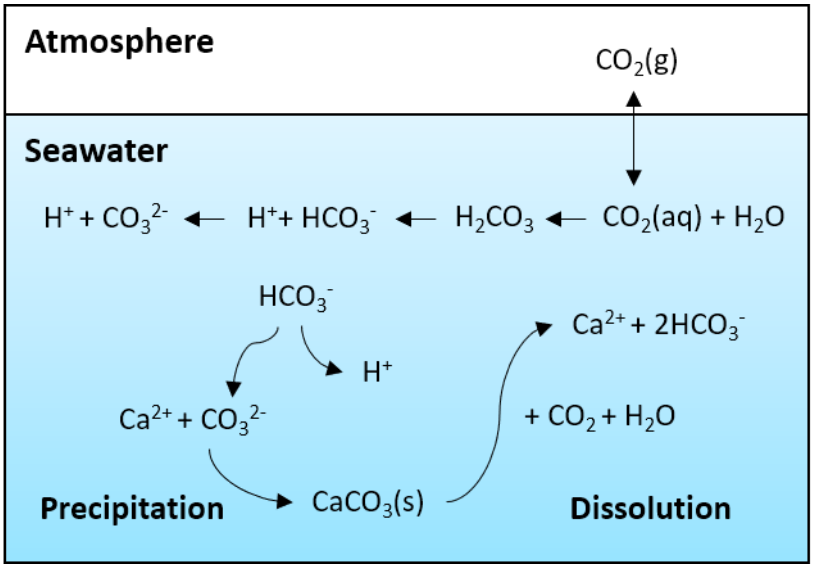

Figure 27 Schematic illustration of carbon dioxide circulation in seawater

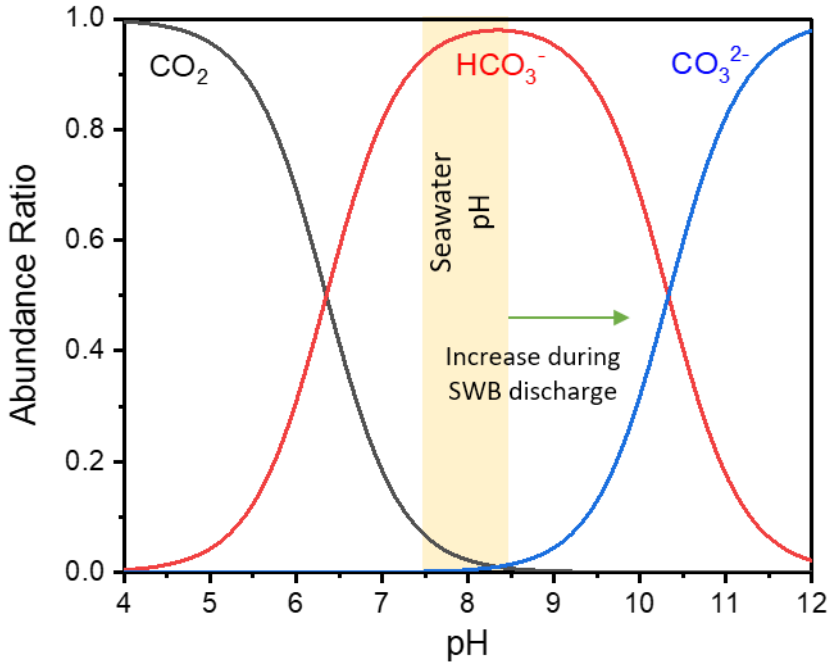

Figure 28 Schematic illustration of carbonic acid equilibria according to pH

To get an insight into the physical effects of calcium carbonate precipitation on the ACC cathode structure, SEM images of the ACC cathode fibers were acquired after discharging the SWB for 20mAh. Fig 29 shows the low and high-resolution SEM images of the ACC fibers before and after discharging, exhibiting crystal precipitates adhered to the surface of the fibers. Coverage of the ACC surface micropores by the precipitates can be observed, which naturally prevents full access of the reactant to the reaction sites, also blocking electron transfer between the fibers *via* the electronic insulating property of calcium carbonate. Additional EDS mapping images from Fig. 30 reveals the atomic composition of the precipitates to be mainly comprised of Ca, C and O species. These results coincide with the previously taken XRD analysis data and confirm that the precipitates formed after the discharge of the SWB are $CaCO_3$ (aragonite phase). Overall, the $CaCO_3$ precipitates formed after discharge can be expected to exert a negative influence on the cell performance, *e.g.*, decrease in the specific surface area and loss of electrical conductivity.

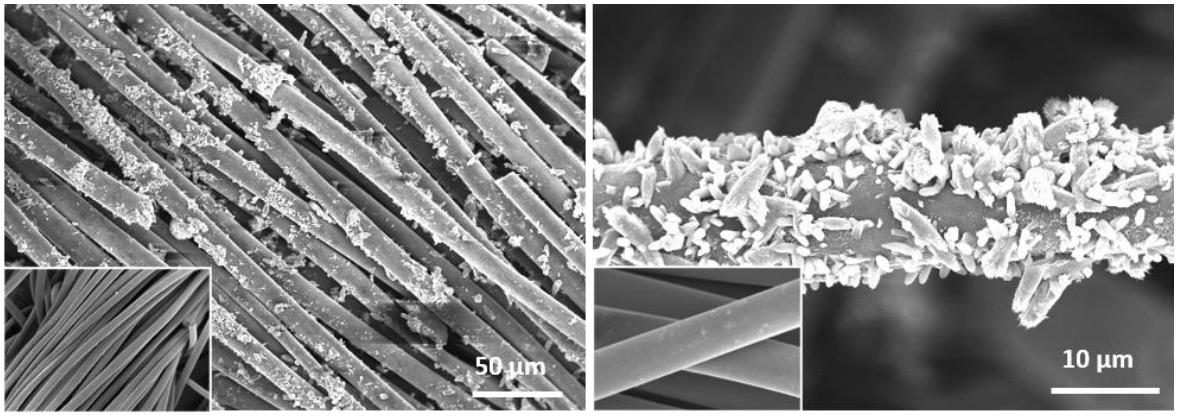

Figure 29 SEM images of 20mAh pre-discharged ACC showing $CaCO_3$ crystal precipitate formation on the fiber surface with inset images of pristine ACC of the same resolution.

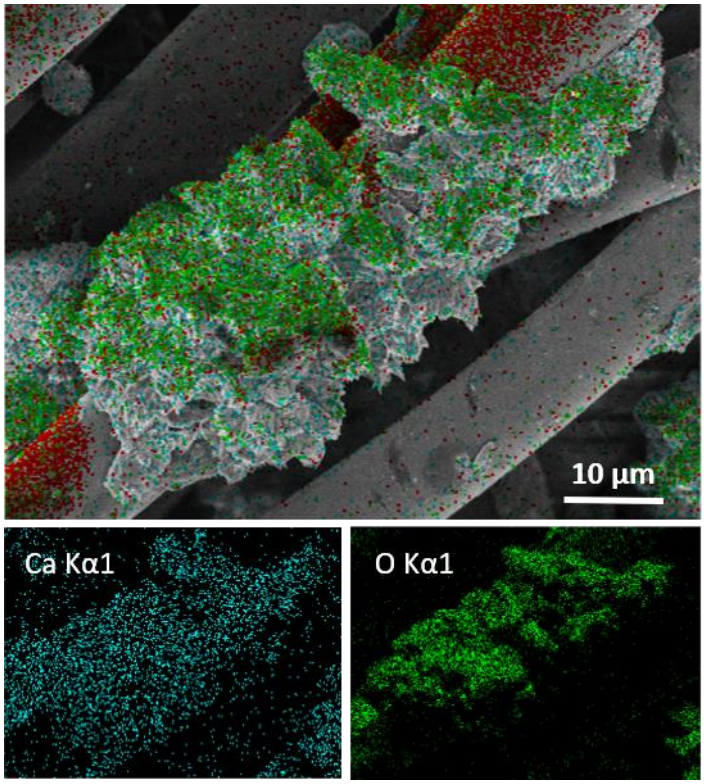

Figure 30 EDS mapping images of discharged ACC showing $CaCO_3$ crystallite surface precipitation.

Nitrogen adsorption/desorption isotherms of the ACC samples before and after discharging are shown in Fig. 31 to examine the effect of CaCO3 precipitation on the BET specific surface area and pore size distribution. The ACC cathode was pre-discharged 20mAh in advance to artificially precipitate more $CaCO_3$ crystals on the surface and compare its characteristics with a pristine ACC sample as previously done for carbon corrosion. By comparing the isotherms of the pristine and pre-discharged ACC, it can be seen that the adsorbed volume significantly decreased after discharging, indicating that $CaCO_3$ precipitation has decreased its specific surface area from $2078 m^2 g^{-1}$ to $1440 m^2 g^{-1}$ and its mean pore diameter from 1.72nm to 1.68nm. This reduction of the surface area is likely due to the coverage of the ACC surface by the $CaCO_3$ precipitates, as seen in the previous SEM images, which will consequently result in the degeneration of the SWB cell performance.

Table 4 Numerical values of the specific surface area, total pore volume, mean pore diameter of the ACC before and after discharging via BET

BET method	Pristine ACC	Discharged ACC
Specific surface area ($m^2 g^{-1}$)	2038	1440
Total pore volume ($cm^3 g^{-1}$)	0.89	0.61
Mean pore diameter (nm)	1.76	1.68

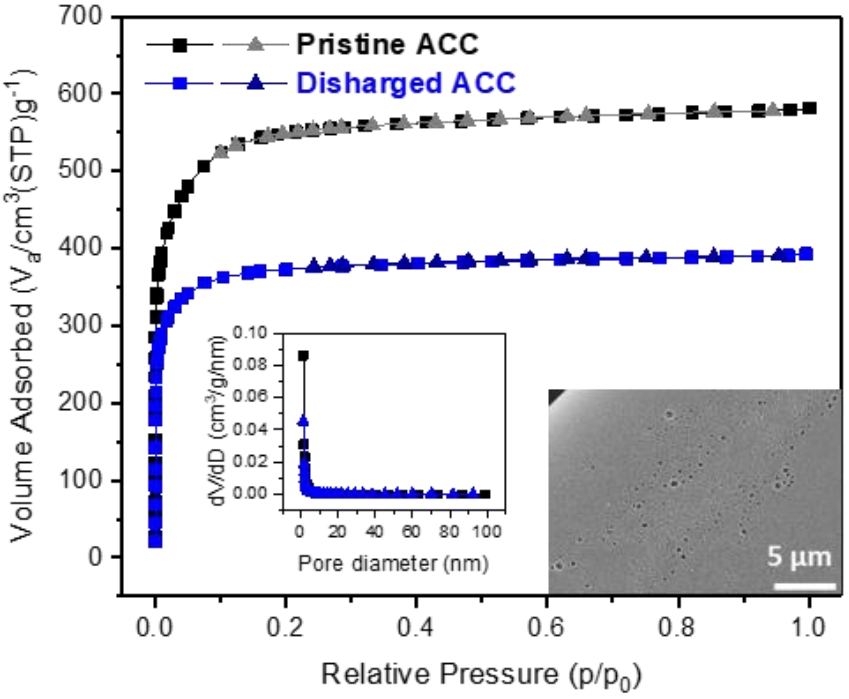

Figure 31 Comparison between pristine and 20mAh discharged ACC by N_2 adsorption-desorption isotherms, pore size distribution (inset)

XPS analysis of the identical discharged sample was carried out to characterize the surface functional groups of the ACC after $CaCO_3$ precipitate formation. Fig. 32 shows the spectra of the ACC cathodes before and after discharging for 20mAh, revealing major C1s and O1s peaks of high intensity and other minor S2p, N1s, Na1s, Mg1s, Ca2s, and Ca2p peaks emerging after discharging. Akin with the previously analyzed XPS data of the charged ACC, a prominent increase of the O1s peak from 4.52% to 29.91% can be observed, along with the mentioned minor peaks originating from the naturally existing ions in residual seawater. Differentiating from the data of the charged ACC, however, the increase in the O1s peak and the new emergence of the calcium species can be attributed to the formation of $CaCO_3$ precipitates on the surface after discharging. In more detail, the precipitates induced higher O and Ca contents, as shown through the XPS surface analysis. These resulting changes of the surface functional groups support the presence of $CaCO_3$ precipitation occurring as a side-reaction during the discharge of the SWB.

Table 5 Numerical values of the carbon, oxygen, and calcium content of the ACC before and after discharging via XPS

Atomic %	Pristine ACC	Discharged ACC
C1s	95.48	57.67
O1s	4.52	29.91
Ca2p	-	3.35

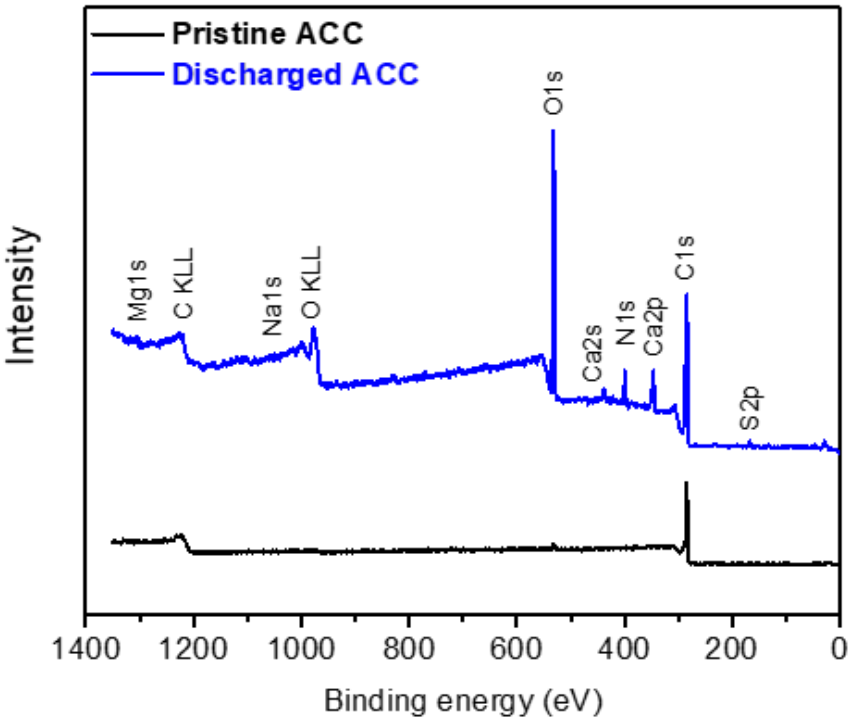

Figure 32 XPS spectra comparison showing calcium species emerging after discharging

The electrochemical performances of the ACC cathode before and after pre-discharging were evaluated by assembling SWB cells for galvanostatic discharge tests. The discharge tests were conducted by applying a current of 0.25mA(0.13mAcm^{-2}) for 5h, and their discharging voltage profiles are shown in Fig. 33. In comparison to the pristine ACC cathode, the 20mAh pre-discharged cathode revealed a deterioration in the cell performance as shown by a decreased discharge voltage plateau, from 2.91V to 2.74V. This increase in the extent of polarization during the discharge procedure indicates that $CaCO_3$ precipitation on the ACC cathode surface induces a negative impact on cell performance. Likewise, as seen from Fig. 34, CV was conducted in a range from -0.5V to 1.0V (vs Ag/AgCl) at a scan rate of 0.2mVs^{-1} to examine the effect of $CaCO_3$ precipitation on the ECSA of the ACC cathode after discharge. In comparison to the pristine ACC cathode, the pre-discharged cathode exhibited a loss of ECSA, although not quite so severe as in the case of the carbon corrosion voltammogram. The apex current density decreases from 0.89mAcm^{-2} to 0.3mAcm^{-2} in OER and increases from -0.72mAcm^{-2} to -0.3mAcm^{-2} in ORR, further indicating the loss of electrochemical activity of the ACC cathode. As previously seen from the SEM images and N2 adsorption-desorption results, $CaCO_3$ precipitation was found to cover the surface of the carbon fiber and consequently lead to surface area loss. The CV results are in correspondence with these previous results, elucidating that $CaCO_3$ precipitation has blocked the access of the reactant to the active sites of the ACC cathode. However, by comparing the CV data of carbon corrosion and $CaCO_3$ precipitation, it can also be observed that carbon corrosion has resulted in a much stronger deterioration of the electrochemical performance than $CaCO_3$ precipitation.

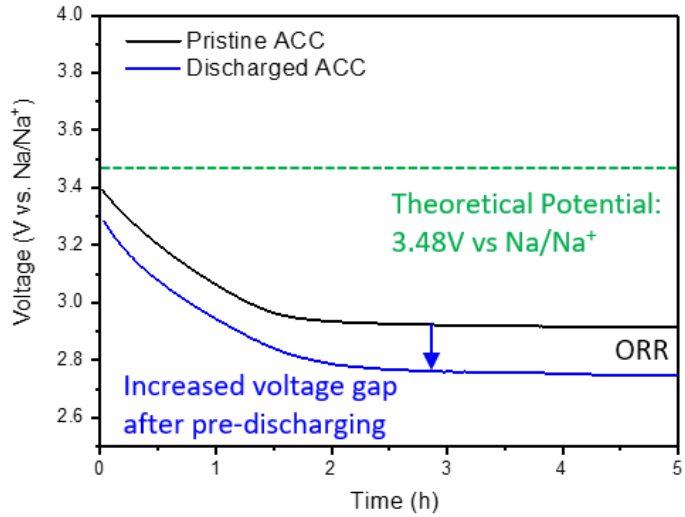

Figure 33 Galvanostatic discharge voltage profile comparison at 0.25mA (0.13mA cm^{-2}) for 5h

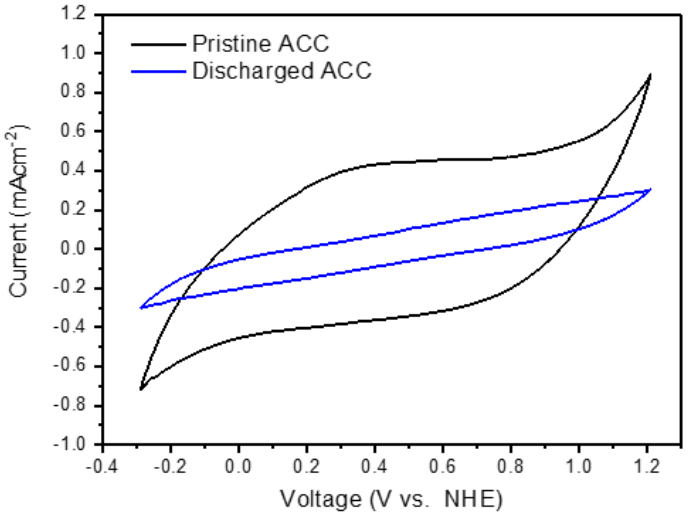

Figure 34 Cyclic voltammograms at a scan rate of 0.2mVs^{-1}

3.3 Side-reactions at actual cycle environments

Carbon corrosion and $CaCO_3$ precipitation at the ACC cathode were identified to occur as side-reactions during the charge and discharge of the SWB. Furthermore, negative impacts on cell performance were found to occur after the artificial aggravation of the corresponding side reactions. In terms of actual operational cycle environments, however, the effects of these cathode side-reactions have yet to be identified.

An experimental setup utilizing two cathodes and a single anode were used as in Fig. 35 and Fig. 36 to clarify the influence of each individual side-reactions during cycling environments. In more detail, this three-electrode setup physically decouples the cathode OER/ORR process so that they occur separately at alternate time intervals in two different ACC cathodes, while at the same time enables them to share the same seawater catholyte during the operation. This experimental architecture thus enables the confinement of each cathode side-reactions into their corresponding cathodes of the SWB at cycling conditions, where the results are shown in Fig. 37. Each ACC cathode was either charged or discharged at a current of 0.25mA(0.13mAcm^{-2}) alternately for 5h, showing pronounced differences in the trend of their voltage plateau. In the case of the charging cathode, a continuous ascending of the voltage plateau can be observed from an initial 3.5V to a final 4.1V after repeated charging, indicating a continual increase in the extent of polarization. Conversely, the discharging cathode maintains a constant voltage plateau of 2.9V even after repeated discharging for over than 50 periods. These results reveal that while carbon corrosion irreversibly deteriorates the cell performance, $CaCO_3$ precipitation is a reversible process that is mitigated during the charge and discharge of the SWB. Consequently, $CaCO_3$ precipitation has no effect on the cell performance.

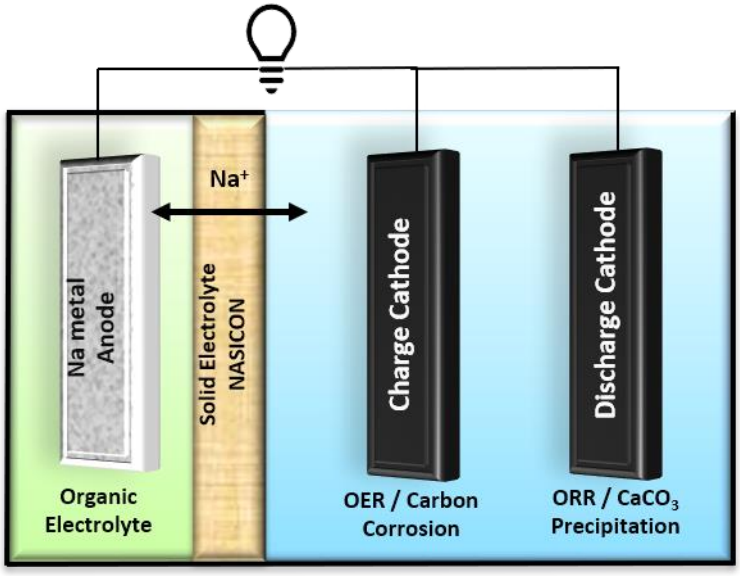

Figure 36 Schematic illustration of the three-electrode cycle experiment setup showing the configuration of the charge cathode / anode / discharge cathode

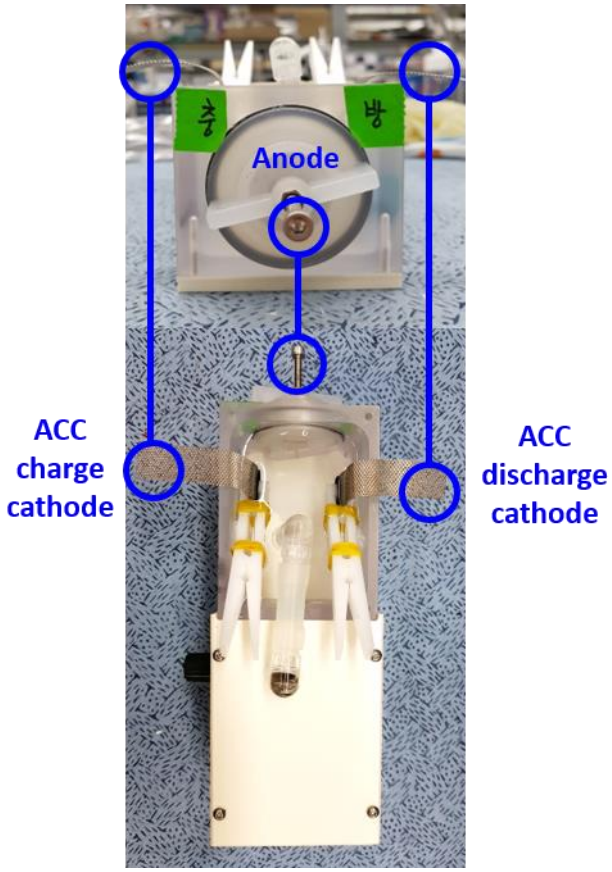

Figure 35 Actual setup of the three-electrode cycle experiment

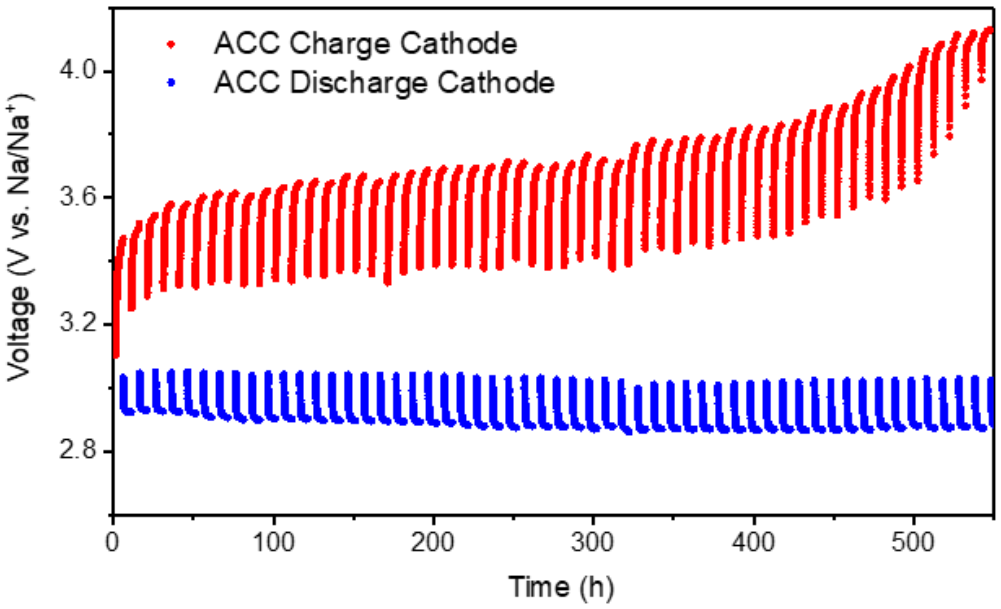

Figure 37 Galvanostatic charge-discharge voltage profiles using the three-electrode cycle setup with physically decoupled cathodes

The causes for this irreversibility of carbon corrosion and reversibility of $CaCO_3$ precipitation is proposed and illustrated as in Fig. 38. Some causes include the pH change of the seawater catholyte during the OER/ORR reaction at Equation (2), during the charge and discharge of the SWB. In more detail, $CaCO_3$ is known to dissolve back to its original state according to the carbonic acid system when pCO2 increases.[49] In terms of electrochemical reactions in the SWB, the pH of the seawater decreases during the charging process due to the OER reaction consuming the hydroxide ions, and conversely increases during the discharging step *via* the ORR reaction producing the hydroxide ions.

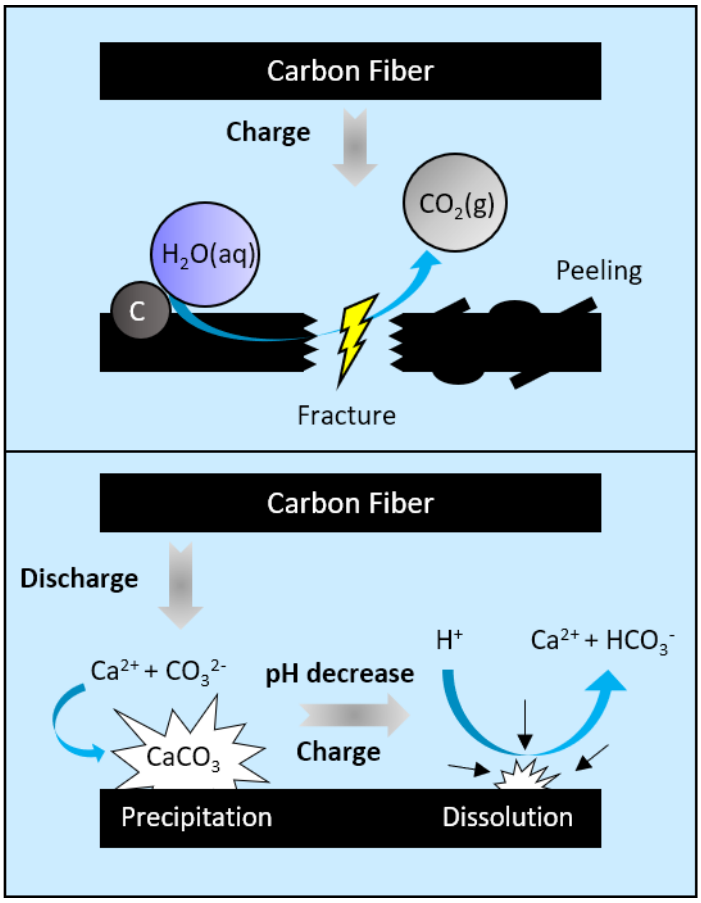

Figure 38 Schematic illustration of carbon corrosion and $CaCO_3$ precipitation/dissolution occurring at the carbon fiber surface during charge-discharge

This procedure is proved in Fig. 39, where the pH of the seawater is *in-situ* tracked during the charge and discharge of the SWB at a current of 0.25mA(0.13mAcm^{-2}) for 5h. The pH of the seawater catholyte can be found to be decreased to a final pH of 6.8 during charging and recovered back to a pH of 7.8 during discharging, showing a tenfold fluctuation in the concentration of H_+ ions, shifting the carbonic acid equilibria from bicarbonate ions to CO_2. SEM and EDS images of the surface fibers after charging the 20mAh pre-discharged ACC with an identical capacity of 20mAh are shown in Fig. 40. The largely reduced amount of precipitates on the surface again reveals that the formed $CaCO_3$ precipitates during discharge are reversibly dissolved back to calcium and bicarbonate ions due to the increased acidity and concentration of hydrogen ions in the seawater catholyte during charging.

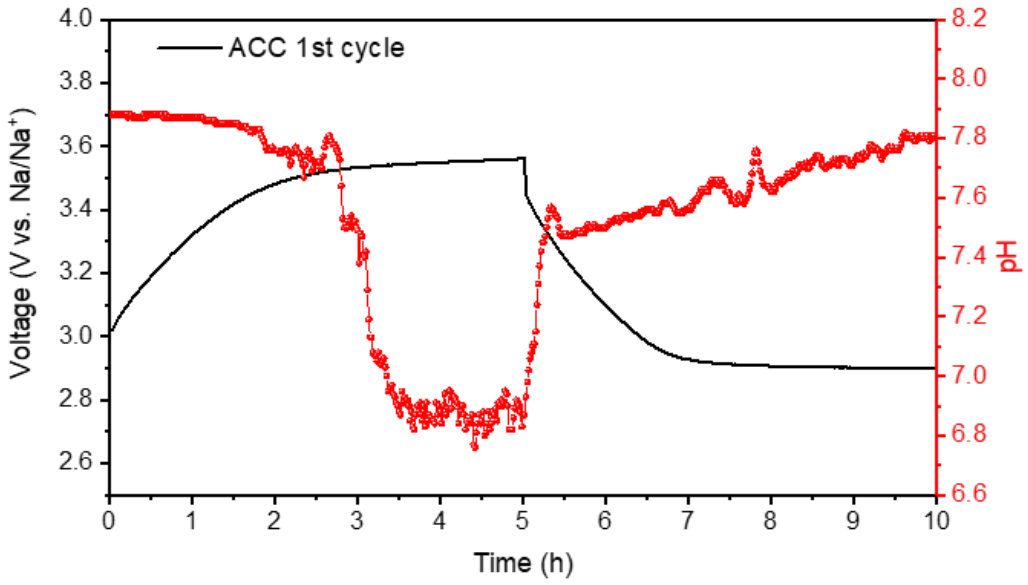

Figure 39 In-situ pH measurement of the seawater catholyte during galvanostatic charge-discharge, both at a current density of 0.25mA (0.13mA cm^{-2}) for 5h

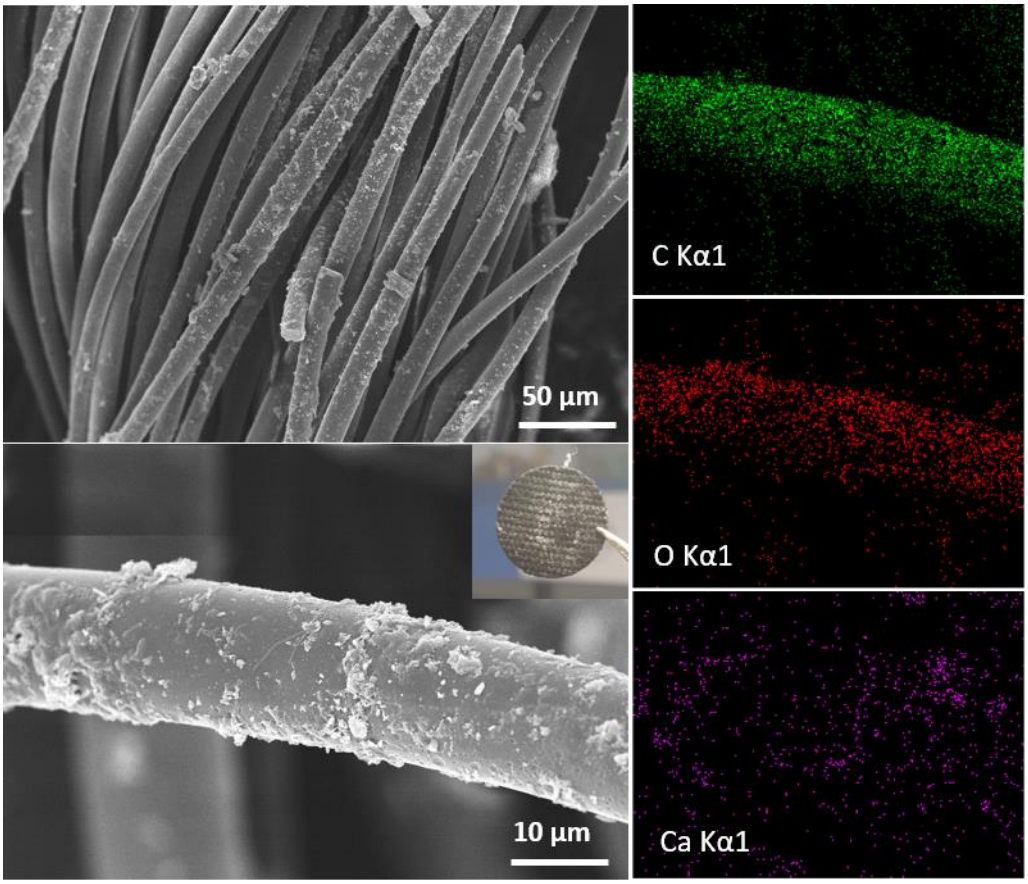

Figure 40 SEM images and the inset photograph of ACC showing removal of $CaCO_3$ precipitates after charging the pre-discharged cathode. EDS mapping images of, showing traces of $CaCO_3$ after charging

3.4 Resistance to side-reactions according to graphitization

Carbon corrosion was identified as the main cause for performance failure in carbonaceous seawater battery cathodes and highlighted the necessity to overcome and suppress the degradation mechanism for lifespan enhancement. In this respect, the morphology of carbon substances was investigated to find an alternative Activated Carbon Felt (ACF) cathode that is suitable for the resistance to carbon corrosion.

In general, graphite-based carbon materials form a layered structure in which the hexagonal network planes composed of sp2 hybridized carbon atoms forming a graphene layer, with the graphene layer planes stacked together via the weakly interacting Van der Waals force. This layered structure of the carbon-based electrode leads to the division into two types of carbon surface: the flat 'Basal Plane' and cross-sectional 'Edge Plane' as illustrated in Fig. 41. It is important to note that the nature of the carbon-based electrode surface greatly changes depending on the pretreatment and surface treatment process, which in this case was the difference between the ACC and ACF cathode. Due to the nature of carbon atoms in the edge plane reacting easily with oxygen or water, which in turn leads to carbon corrosion, the ratio of the basal plane to the edge plane (eg. Degree of graphitization) needs to be considered.

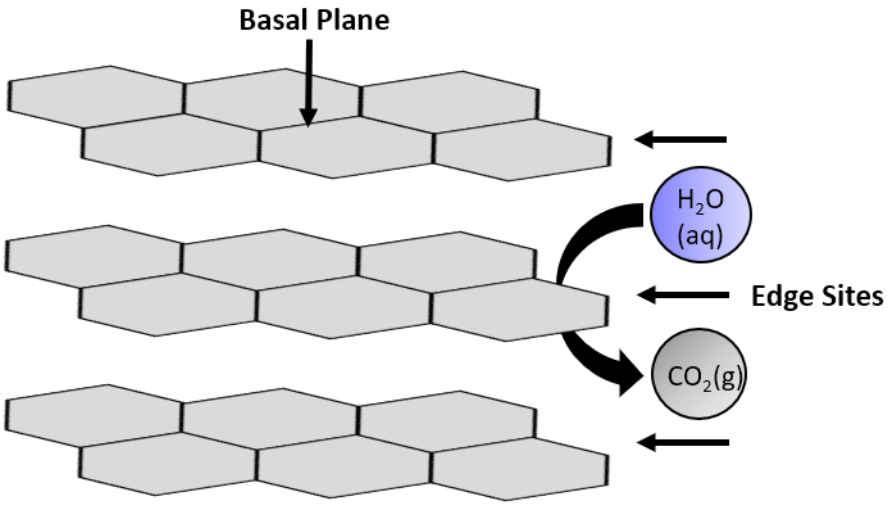

Figure 41 Schematic of the basal planes and edge sites of the carbon surface

Raman analysis was conducted to compare the degree of graphitization in the ACC and ACF cathode via the I_d/I_g band ratio. The I_g band corresponds to the 1582 cm^{-1} band of graphite known as the G band, with the I_d band corresponding to the 1350 cm^{-1} band known as the D band. This difference rises from the fact that graphite is composed of sp^2 bonded carbon in planar sheets in which the bond energy of the sp^2 bonds is higher than the sp^3 bonds of diamond. The intensity ratio I_d/I_g thus helps to estimate the defects of carbon-based materials, with the degree of graphitization increasing as the ratio becomes smaller. Results from the Raman spectra comparing the ACC and ACF showed an I_d/I_g band ratio of 1.02 and 0.92 respectively and are shown in Fig. 42 and Fig. 43. The alternative ACF is thus found to have a more graphitic nature in comparison to the ACC, which leads to the estimation that it will have more resistance to carbon corrosion.

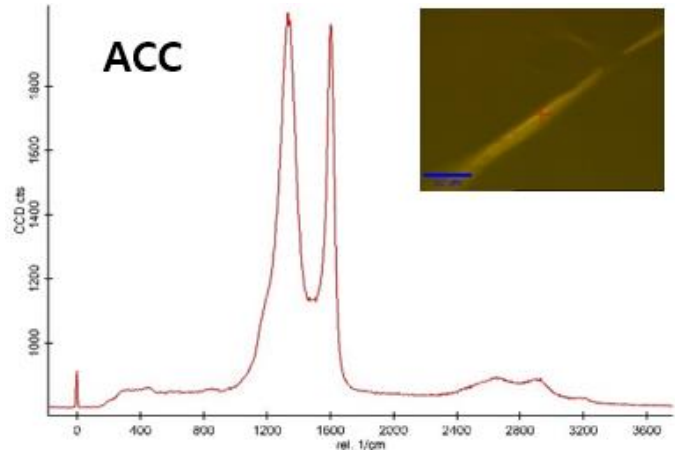

Figure 43 Raman spectra of the activated carbon cloth showing I_d/I_g peaks

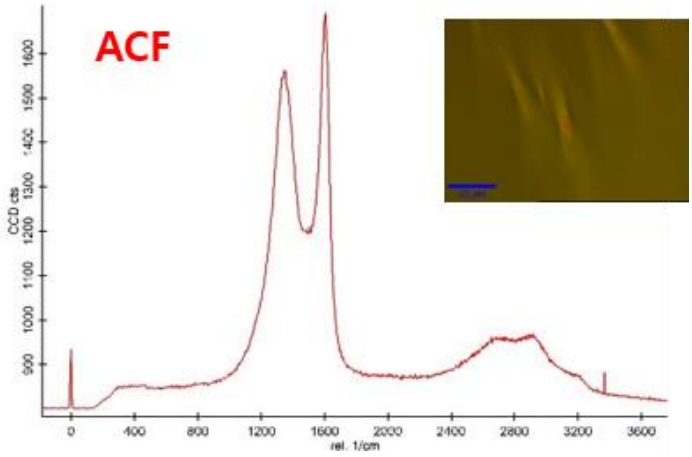

Figure 42 Raman spectra of the activated carbon felt showing I_d/I_g peaks

Carbon corrosion resistance of the ACC and ACF was compared by monitoring the gas evolution with DEMS during the galvanostatic charging of the SWB cell at a current of 0.25mA ($0.13mAcm^{-2}$), as shown in Fig. 44. The resulting CO_2 gas evolution suppression of the ACF shows that its graphitic nature likely contributed towards to reduction of CO_2 gas evolution.

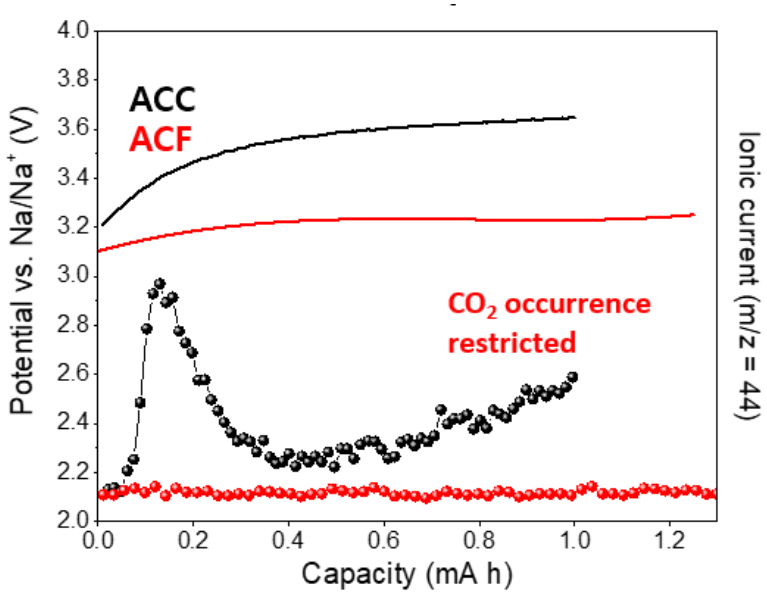

Figure 44 DEMS comparison between ACC and ACF showing carbon corrosion resistance

Cycle life comparison was done via galvanostatic charge-discharge at a current of 0.25mA (0.13mAcm^{-2}) for 5h at each step and are shown in Fig. 46. The ACF cathode exhibited a smaller initial voltage gap (0.46V) and a longer life cycle (100 cycles) at a discharge voltage cut-off of 2.5V in comparison to the ACC (0.6V and 80 cycles). Polarization curves were also fitted with a current scan rate of 1uA/s and are shown in Fig. 45. The resulting peak power difference showed that the ACF (9mW) exceeded the performance of the ACC (7.3mW), overall leading to the conclusion that the ACF has better properties than the ACC in terms of carbon corrosion resistance, voltage efficiency, cycle life, and power output.

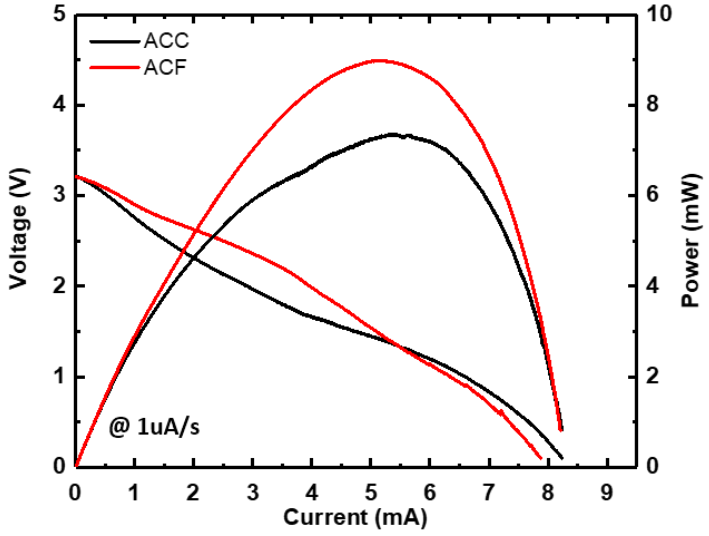

Figure 46 Comparison between ACC and ACF polarization curves showing peak power difference

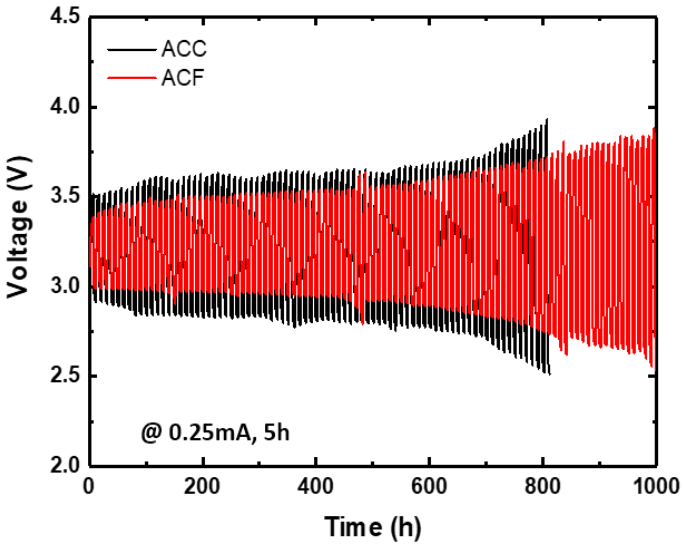

Figure 45 Comparison between ACC and ACF cycle performance at a current density of 0.13mAcm^{-2}

IV. Conclusion

In the present study, carbon corrosion occurring as a cathode side-reaction during charging was identified and pointed out as the main cause for performance failure in SWBs. Carbon corrosion and $CaCO_3$ precipitation were found to unwantedly occur at the ACC cathode during charge and discharge, as identified via DEMS and XRD analyses. Both side-reactions were confirmed to give a negative impact on the electrochemical SWB performance when intensified in advance, resulting in a voltage plateau increase from 3.51V to 3.66V by carbon corrosion and decrease from 2.91V to 2.74V by $CaCO_3$ precipitation. A three-electrode experimental setup was used to ascertain the impact of each cathode side-reactions during actual cell operation, revealing the reversibility of $CaCO_3$ precipitation and the irreversibility of carbon corrosion. Based on these results, it can be concluded that the prevention of the irreversible carbon corrosion at the cathode can lead to increased voltage efficiency and cycle stability for SWBs and are summarized in Fig. 47. Further enhancements by the application of more optimal carbon electrode materials showed the suppression of carbon corrosion in SWB systems, and further elongated the performance and operational lifespan. Optimal OER catalyst application can also be considered as a method to further enhance the performance and stability of the SWB cathode.[50, 51]

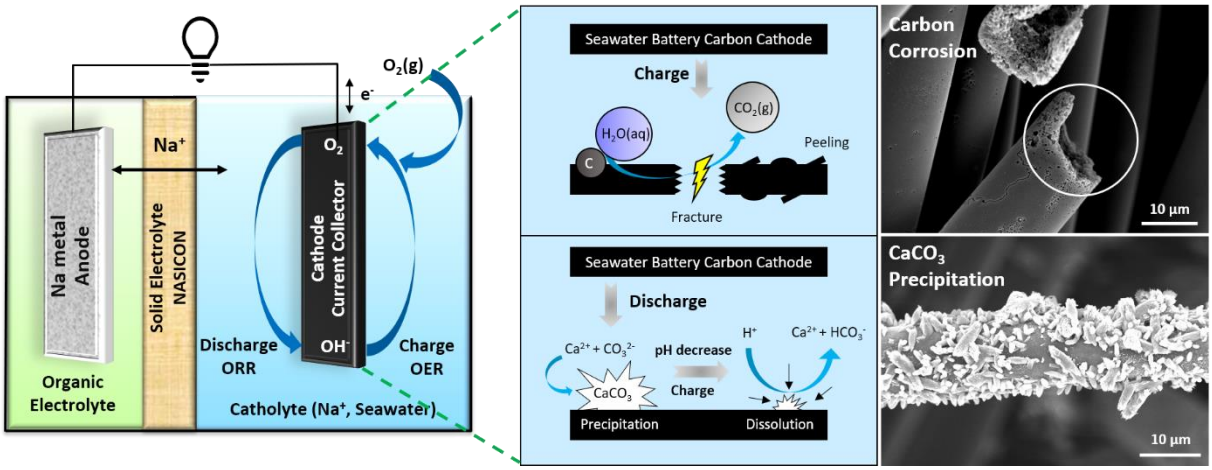

Figure 47 Summary of the side-reactions occurring in carbonaceous seawater batteries, with CaCO3 precipitation as a reversible phenomenon and Carbon Corrosion as an irreversible phenomenon

V. Reference

1. Larcher, D.; Tarascon, J. M., Towards greener and more sustainable batteries for electrical energy storage. *Nature Chemistry* **2015,** *7* (1), 19-29.

2. Nair, N.-K. C.; Garimella, N., Battery energy storage systems: Assessment for small-scale renewable energy integration. *Energy and Buildings* **2010,** *42* (11), 2124-2130.

3. Poizot, P.; Dolhem, F., Clean energy new deal for a sustainable world: from non-CO2 generating energy sources to greener electrochemical storage devices. *Energy & Environmental Science* **2011,** *4* (6), 2003-2019.

4. Yang, Z.; Zhang, J.; Kintner-Meyer, M. C. W.; Lu, X.; Choi, D.; Lemmon, J. P.; Liu, J., Electrochemical Energy Storage for Green Grid. *Chemical Reviews* **2011,** *111* (5), 3577-3613.

5. Holzinger, C.; Pelletier, T.; Grejtak, T.; Robinson, C., Global Energy Storage Market Forecast 2019. *Lux Research* **2020**.

6. Nikolaidis, P.; Poullikkas, A., A comparative review of electrical energy storage systems for better sustainability. *Journal of Power Technologies* **2017**.

7. Mouli-Castillo, J.; Wilkinson, M.; Mignard, D.; McDermott, C.; Haszeldine, R. S.; Shipton, Z. K., Inter-seasonal compressed-air energy storage using saline aquifers. *Nature Energy* **2019,** *4* (2), 131-139.

8. Krack, M.; Secanell, M.; Mertiny, P., Rotor design for high-speed flywheel energy storage systems. *Energy Storage in the Emerging Era of Smart Grids* **2011**, 41.

9. Hannan, M.; Hoque, M.; Mohamed, A.; Ayob, A., Review of energy storage systems for electric vehicle applications: Issues and challenges. *Renewable and Sustainable Energy Reviews* **2017,** *69*, 771-789.

10. Kim, J.; Park, H., Experimental analysis of discharge characteristics in vanadium redox flow battery. *Applied Energy* **2017,** *206*, 451-457.

11. Qi, W.; Shapter, J. G.; Wu, Q.; Yin, T.; Gao, G.; Cui, D., Nanostructured anode materials for lithium-ion batteries: principle, recent progress and future perspectives. *Journal of Materials Chemistry A* **2017,** *5* (37), 19521-19540.

12. Bruce, P. G.; Scrosati, B.; Tarascon, J.-M., Nanomaterials for Rechargeable Lithium Batteries. *Angewandte Chemie International Edition* **2008,** *47* (16), 2930-2946.

13. Goodenough, J. B.; Park, K.-S., The Li-Ion Rechargeable Battery: A Perspective. *Journal of the American Chemical Society* **2013,** *135* (4), 1167-1176.

14. Kang, K.; Meng, Y. S.; Bréger, J.; Grey, C. P.; Ceder, G., Electrodes with High Power and High Capacity for Rechargeable Lithium Batteries. *Science* **2006,** *311* (5763), 977.

15. Scrosati, B., Recent advances in lithium ion battery materials. *Electrochimica Acta* **2000,** *45* (15), 2461-2466.

16. Scrosati, B.; Garche, J., Lithium batteries: Status, prospects and future. *Journal of Power Sources* **2010,** *195* (9), 2419-2430.

17. Grosjean, C.; Miranda, P. H.; Perrin, M.; Poggi, P., Assessment of world lithium resources and consequences of their geographic distribution on the expected development of the electric vehicle industry. *Renewable and Sustainable Energy Reviews* **2012,** *16* (3), 1735-1744.

18. Gruber, P. W.; Medina, P. A.; Keoleian, G. A.; Kesler, S. E.; Everson, M. P.; Wallington, T. J., Global Lithium Availability. *Journal of Industrial Ecology* **2011,** *15* (5), 760-775.

19. Olivetti, E. A.; Ceder, G.; Gaustad, G. G.; Fu, X., Lithium-Ion Battery Supply Chain Considerations: Analysis of Potential Bottlenecks in Critical Metals. *Joule* **2017,** *1* (2), 229-243.

20. Kim, Y.; Hwang, S. M.; Yu, H.; Kim, Y., High energy density rechargeable metal-free seawater batteries: a phosphorus/carbon composite as a promising anode material. *Journal of Materials Chemistry A* **2018,** *6* (7), 3046-3054.

21. Hwang, S. M.; Park, J.-S.; Kim, Y.; Go, W.; Han, J.; Kim, Y.; Kim, Y., Rechargeable Seawater Batteries—From Concept to Applications. *Advanced Materials* **2019,** *31* (20), 1804936.

22. Kim, J.-K.; Mueller, F.; Kim, H.; Bresser, D.; Park, J.-S.; Lim, D.-H.; Kim, G.-T.; Passerini, S.; Kim, Y., Rechargeable-hybrid-seawater fuel cell. *NPG Asia Materials* **2014,** *6* (11), e144-e144.

23. Senthilkumar, S. T.; Go, W.; Han, J.; Pham Thi Thuy, L.; Kishor, K.; Kim, Y.; Kim, Y., Emergence of rechargeable seawater batteries. *Journal of Materials Chemistry A* **2019,** *7* (40), 22803-22825.

24. Park, J.; Park, J.-S.; Senthilkumar, S. T.; Kim, Y., Hybridization of cathode electrochemistry in a rechargeable seawater battery: Toward performance enhancement. *Journal of Power Sources* **2020,** *450*, 227600.

25. Zhang, Y.; Park, J.-S.; Senthilkumar, S. T.; Kim, Y., A novel rechargeable hybrid Na-seawater flow battery using bifunctional electrocatalytic carbon sponge as cathode current collector. *Journal of Power Sources* **2018,** *400*, 478-484.

26. Avasarala, B.; Moore, R.; Haldar, P., Surface oxidation of carbon supports due to potential cycling under PEM fuel cell conditions. *Electrochimica Acta* **2010,** *55* (16), 4765-4771.

27. Cai, M.; Ruthkosky, M. S.; Merzougui, B.; Swathirajan, S.; Balogh, M. P.; Oh, S. H., Investigation of thermal and electrochemical degradation of fuel cell catalysts. *Journal of Power Sources* **2006,** *160* (2), 977-986.

28. Maass, S.; Finsterwalder, F.; Frank, G.; Hartmann, R.; Merten, C., Carbon support oxidation in PEM fuel cell cathodes. *Journal of Power Sources* **2008,** *176* (2), 444-451.

29. Oh, H.-S.; Oh, J.-G.; Haam, S.; Arunabha, K.; Roh, B.; Hwang, I.; Kim, H., On-line mass spectrometry study of carbon corrosion in polymer electrolyte membrane fuel cells. *Electrochemistry Communications* **2008,** *10* (7), 1048-1051.

30. Park, J.; Oh, H.; Ha, T.; Lee, Y. I.; Min, K., A review of the gas diffusion layer in proton exchange membrane fuel cells: Durability and degradation. *Applied Energy* **2015,** *155*, 866-880.

31. Roen, L. M.; Paik, C. H.; Jarvi, T. D., Electrocatalytic Corrosion of Carbon Support in PEMFC Cathodes. *Electrochemical and Solid-State Letters* **2004,** *7* (1), A19.

32. Tang, H.; Qi, Z.; Ramani, M.; Elter, J. F., PEM fuel cell cathode carbon corrosion due to the formation of air/fuel boundary at the anode. *Journal of Power Sources* **2006,** *158* (2), 1306-1312.

33. Wang, J.; Yin, G.; Shao, Y.; Zhang, S.; Wang, Z.; Gao, Y., Effect of carbon black support corrosion on the durability of Pt/C catalyst. *Journal of Power Sources* **2007,** *171* (2), 331-339.

34. Derr, I.; Fetyan, A.; Schutjajew, K.; Roth, C., Electrochemical analysis of the performance loss in all vanadium redox flow batteries using different cut-off voltages. *Electrochimica Acta* **2017,** *224*, 9-16.

35. Eifert, L.; Banerjee, R.; Jusys, Z.; Zeis, R., Characterization of Carbon Felt Electrodes for Vanadium Redox Flow Batteries: Impact of Treatment Methods. *Journal of The Electrochemical Society* **2018,** *165* (11), A2577-A2586.

36. Liu, H.; Xu, Q.; Yan, C., On-line mass spectrometry study of electrochemical corrosion of the graphite electrode for vanadium redox flow battery. *Electrochemistry Communications* **2013,** *28*, 58-62.

37. Liu, H.; Xu, Q.; Yan, C.; Qiao, Y., Corrosion behavior of a positive graphite electrode in vanadium redox flow battery. *Electrochimica Acta* **2011,** *56* (24), 8783-8790.

38. Trogadas, P.; Taiwo, O. O.; Tjaden, B.; Neville, T. P.; Yun, S.; Parrondo, J.; Ramani, V.; Coppens, M.-O.; Brett, D. J. L.; Shearing, P. R., X-ray micro-tomography as a diagnostic tool for the electrode degradation in vanadium redox flow batteries. *Electrochemistry Communications* **2014,** *48*, 155-159.

39. Hasvold, Ø.; Henriksen, H.; Melv┤r, E.; Citi, G.; Johansen, B. Ø.; Kjønigsen, T.; Galetti, R., Sea-water battery for subsea control systems. *Journal of Power Sources* **1997,** *65* (1), 253-261.

40. Shinohara, M.; Araki, E.; Mochizuki, M.; Kanazawa, T.; Suyehiro, K., Practical application of a sea-water battery in deep-sea basin and its performance. *Journal of Power Sources* **2009,** *187* (1), 253-260.

41. Kang, S. J.; Mori, T.; Narizuka, S.; Wilcke, W.; Kim, H.-C., Deactivation of carbon electrode for elimination of carbon dioxide evolution from rechargeable lithium–oxygen cells. *Nature*

Communications **2014,** *5* (1), 3937.

42. McCloskey, B. D.; Bethune, D. S.; Shelby, R. M.; Girishkumar, G.; Luntz, A. C., Solvents' Critical Role in Nonaqueous Lithium–Oxygen Battery Electrochemistry. *The Journal of Physical Chemistry Letters* **2011,** *2* (10), 1161-1166.

43. Colmenares, L. C.; Wurth, A.; Jusys, Z.; Behm, R. J., Model study on the stability of carbon support materials under polymer electrolyte fuel cell cathode operation conditions. *Journal of Power Sources* **2009,** *190* (1), 14-24.

44. Gallagher, K. G.; Fuller, T. F., Kinetic model of the electrochemical oxidation of graphitic carbon in acidic environments. *Physical Chemistry Chemical Physics* **2009,** *11* (48), 11557-11567.

45. Leofanti, G.; Padovan, M.; Tozzola, G.; Venturelli, B., Surface area and pore texture of catalysts. *Catalysis Today* **1998,** *41* (1), 207-219.

46. Bae, H.; Park, J.-S.; Senthilkumar, S. T.; Hwang, S. M.; Kim, Y., Hybrid seawater desalination-carbon capture using modified seawater battery system. *Journal of Power Sources* **2019,** *410-411*, 99-105.

47. Dean, J. A., *Lange's handbook of chemistry*. New york; London: McGraw-Hill, Inc.: 1999.

48. Haynes, W. M., *CRC handbook of chemistry and physics*. CRC press: 2014.

49. Morse, J. W.; Arvidson, R. S.; Lüttge, A., Calcium Carbonate Formation and Dissolution. *Chemical Reviews* **2007,** *107* (2), 342-381.

50. Jang, S.-E.; Kim, H., Effect of Water Electrolysis Catalysts on Carbon Corrosion in Polymer Electrolyte Membrane Fuel Cells. *Journal of the American Chemical Society* **2010,** *132* (42), 14700-14701.

51. Oh, J.-G.; Lee, W. H.; Kim, H., The inhibition of electrochemical carbon corrosion in polymer electrolyte membrane fuel cells using iridium nanodendrites. *International Journal of Hydrogen Energy* **2012,** *37* (3), 2455-2461.

VI. Acknowledgements

2년간의 대학원 석사생활의 하루 하루는 나름 길게 느껴졌는데 뒤돌아보니 시간이 정말 빨리 지나게 된 것 같습니다. 돌이켜보면 유니스트 학부생 4년, 군대 2년, 대학원 석사과정 2년 동안의 시간이 전부 빠르게 지나갔고, 아직은 졸업을 한다는 것이 크게 와 닿지 않아서 졸업에 대한 현실감이 사실 지금도 없고 심란한 마음만 있는 것 같습니다. 학부생 수업에서 우연한 계기로 해수전지를 연구하는 김영식 교수님을 알게 되었고, 6개월의 인턴십에 이어 대학원 진학을 결심하자 감사하게도 김영식 교수님께서는 저의 대학원 지도교수님이 되어 주셨습니다. 석사과정 중 많은 것들을 지도해주시고 스스로 성장할 수 있는 계기를 마련해주신 김영식 교수님께 감사의 말씀 올립니다. 이어, 저희 YK Research 연구그룹의 구성원들에게 감사를 전하고 싶습니다. 해수전지 양극팀의 수장이었고 박사 졸업 후 포투원 CTO으로 가서 항상 같이 있는 듯한 정선이형, 이제는 미국으로 갔지만 헬스의 세계를 처음 알려주신 현우형, 코로나 자가격리 때문에 결혼식에 참석 못한 영준이형, 그룹에 처음 올때부터 지역활력프로젝트 때문에 항상 고생하시는 왕근이형 등 박사님들 덕분에 많은 웃음을 받을 수 있었습니다. 처음 랩실 컨택할 때 랩장이었고 이제는 아빠가 된 현태형, 연구할 때 프로페셔널함이 무엇인지를 보여주는 우석형, 처음 들어왔을 때 같이 양극팀에서 일했으나 1달만에 미국으로 떠나간 제희, 코로나 전 까지만 해도 헬스장 팟 고정 멤버였던 영진이형, 제희 대신 양극팀 일 처음 정말 많이 도와주고 격려해 주셔서 항상 고마운 진호형, 현 랩장이자 얼마 전까지만 해도 유일한 동갑이었던 우리 뚝배기 브레이커 영재, 늦게까지 항상 남아있는 연구열정 넘치는 남혁형, 석사 입학 동기님으로 같이 자주 으쌰으쌰 했지만 박사의 강을 건너가버린 세영이, 듬직한 탱커역할을 하고 묵묵히 일 잘하는 도완이, 담당 인턴때의 순수한 느낌이 아직도 있고 고생 많이 하는 준호, 베데스다의 추억을 두고두고 회자하고 있는 우리 뚝배기 전담반 종우, 영재에 이어 신흥 먹방 강자로 등장하고 있는 중섭이, 아직 연구원 신분이지만 이미 랩실 사람이나 다름없는 학식러버 성우형, 이제 신입생으로 들어오는 동갑내기 3인방 서해 정우 광호, 말년인 나랑 같이 신설 모듈팀에 들어와서 일하느라 고생하고 있는 우리 동엽이랑 지훈이, 많은 이야기는 못했지만 자주 다가와주고 도와주려 해서 고마운 Sahar와 Ahmad, 다들 잊지 못할 것 같습니다. 마지막으로 해외에 있어 자주 못보지만 항상 조언해주고 응원해주는 우리 가족들, 이제 앞으로 더 듬직한 아들이 되도록 하겠습니다.

감사합니다.